Modelling, Simulations and Characterization of nanoelectromechanical accelerometers based on graphene

Master Thesis
submitted to the Faculty of the
Escola Tècnica d'Enginyeria de Telecomunicació de Barcelona
Universitat Politècnica de Catalunya
by

Daniel Moreno

In partial fulfillment
of the requirements for the master in
ELECTRONIC ENGINEERING (MEE)

Advisor: Guillermo Villanueva
co-Advisor: Ramon Bragós
Barcelona, 31st August 2020

Acknowledgements

This project has been completed thanks to the continuous guidance of Prof. Guillermo Villanueva. He proposed the initial idea for this project and has been actively supervising its development. I would like to thank him for the effort he put in making sure I did not only find the correct way but learnt and understood everything along the way.

I would like to thank my thesis co-advisor, Prof. Ramon Bragós for introducing me to the microelectronics world and for his guidance throughout the thesis.

I would also like to thank KTH researcher Xuge Fan and Prof. Frank Niklaus for the fruitful discussions and the opportunity of using their accelerometers.

Many thanks to the entire ANEMS group at EPFL, particularly to Soumya for the COMSOL help and to Damien for his support in the laboratory.

I want to thank Dr. Cristina Martín for her kindness and wonderful measurements taken with the AFM at SICHH (Fribourg).

Last but not least, I appreciate the support that my family has given me at a distance. Also, special thanks for the constant support that Elena has given me during these months. The sum of master thesis plus lockdown would have been explosive without her.

Lausanne, 31st August 2020

Abstract

Accelerometers are widely used in industrial applications and consumer electronics. We can find them in automotive crash detection or fitness trackers. The majority are based on piezoresistive or capacitive effect which are limited by their large size. This negatively influences their utility in emerging applications such as Internet of Things and biomedical applications.
NEMS (Nanoelectromechanical systems) are presented as a possible solution for this problem. The accelerometers used in this project are made of a suspended graphene membrane and an attached silicon proof mass. They were fabricated by KTH researchers [1]. We study the possibility of measuring accelerations by monitoring the changes in the device resonant frequency. If proven, to the best of our knowledge, they would be the first ultra-miniaturized and sensitive resonant accelerometer.
To do so, we built a functioning model of the accelerometers by combining a theoretical framework and finite element simulations. The chip was placed on a piezo-shaker and measurements were conducted using a Laser Doppler Vibrometer. To complement the study, further measures were taken with an Atomic Force Microscope and a Digital Holographic Microscope.
The results show a good match between theory and simulations. However, the acceleration measurements in the device show higher signals not related with accelerations. We proved they were related to displacements and theorized that they were caused by internal chip forces. Horizontal forces on the accelerometer frame could eclipse the effect of the accelerations on the resonant frequency. We suggest the use of a more rigid chip frame as a potential solution.

Key words: Graphene, Accelerometer, Resonator

Contents

1 Introduction

An accelerometer is an electromechanical device able to measure acceleration forces. These forces can be constant and static (like Earth's gravity) or they can be caused by moving or by vibrating the accelerometer. Targeting the dynamic accelerations, MEMS (Micro Electromechanical Systems) accelerometers have been largely used in automotive applications, where they are used for crash detection and vehicle stability systems [2]. Additionally, due to their small size and light weight, they are used in biomedical and robotics applications for active motion monitoring. They can also be found in the field of consumer electronics inside smartphones to stabilize pictures while using the camera.

In the literature, different kinds of accelerometers have been reported so far, with working principles based on piezoresistive effect, capacitance, tunnelling effect and so on. However, the majority of accelerometers use capacitors or piezoresistors as they have a simple structure and allow batch-fabrication process. Their biggest disadvantage is their larger size, which negatively influences their utility in emerging applications such as the IoT (Internet of Things) that require miniaturized sensors and actuators.

Nowadays, accelerometers with a reduced chip size are needed. Indeed, small, lightweight accelerometers are necessary for many portable devices, biomedical applications, space navigation systems, automobile applications, motion control systems and so on. The biggest challenge is to maintain the sensitivity of the accelerometer as the chip size is decreased.

In this research project, we are addressing this challenge by exploring the possibility of detecting accelerations with the World's smallest accelerometer [3]. These devices were fabricated by X. Fan and F. Niklaus [1] and they proved to read accelerations by measuring the changes in resistivity. In this research study, the same devices are used and accelerations are measured with a different concept. To achieve that, theoretical analysis, simulations and measurements are performed.

1.1 Motivation and Problem statement

The existing resonant MEMS accelerometers are typically large, in the order of several square millimeters. The creation of ultraminiturized accelerometers that could sense wide frequency ranges and have good stability in mechanical operation is critical for emerging applications. They could be useful in wearable electronics, biomedical implants, nanoscale robotics and internet of things (IoT).

The majority of accelerometers are equipped with a proof mass that moves with acceleration forces. Downscaling the accelerometer means reducing the size of the proof mass, which can imply a reduced sensitivity.

1.2 Current technologies and research

Since its discovery, reported by Novoselov et al. [4] in 2004, graphene has attracted attention due to its unusual two-dimensional structure. Additionally, graphene reported wonderful properties such as high Young's modulus, high resonant frequency and unique electrical behaviour.

Suspended graphene structures are used as resonators. Since graphene is atomically thin, its resonant frequency is dominated by in-plane tension, which can be modified electrostatically by applying DC voltage. This means that the resonant frequency can be tuned. Many graphene mechanical resonators have been reported during the past years, built with doubly or fully clamped layers of graphene, allowing resonant frequencies around 100 MHz [5].

Later, the idea was expanded by attaching a mass to the suspended graphene membranes [1]. Accelerations could be measured by reading the change in the electrical resistance of graphene because of the piezoresistivity of the graphene.

In the present study, the fully clamped graphene membranes with suspended silicon proof masses are used as resonators. This means that accelerations are measured by monitoring the changes that the acceleration produces in the resonant frequency of the device.

Until the day of writing these lines, ultra-miniaturized and sensitive resonant accelerometers have not yet been demonstrated.

1.3 Objectives

This research project studies suspended graphene membrane devices which have a proof mass. The main objective is to measure accelerations through the changes in resonant frequency.

To have a complete understanding, the problem is studied from different perspectives. First, the theoretical approach explores how external accelerations create shifts in the resonant

frequency of the system. Later, finite element simulations complete the model. Finally, measurements are performed and compared with the theory and simulations.

1.4 Work Plan

The work plan followed during the research project was heavily influenced by the unexpected COVID-19 lockdown. All the measurements on the devices programmed for that period had to be postponed to June. During lockdown, the theoretical model and simulations were developed working remotely from Switzerland.

Figure 1.1 shows a Gantt diagram on how the time was organized to address the objectives for the theory, simulations and measurements. The project started at the beginning of February 2020 and was completed by the middle of August 2020. As a result, it had a total duration of 27 weeks.

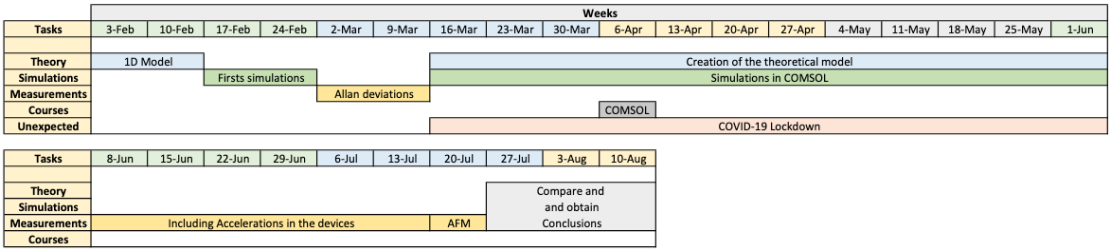

Figure 1.1 – Gantt diagram representing the work plan of the research project. The time was split in Theory, Simulations, Measurements and Courses.

1.5 Thesis structure

Chapter 2. Devices

Description of the accelerometers studied in the research project. Introduction to the language used in the project to designate the devices depending on their proof mass size.

Chapter 3. Analytical Model

Analytical study to obtain the theoretical resonant frequency shift when the devices are under acceleration forces. Definition of the Responsivity parameter used to materialize the acceleration sensing capabilities of the devices.

Chapter 4. Finite Element Simulations

Finite Element Simulations are performed to simulate the devices and visualize the effect of the different parameters. *Static simulations* allowed to obtain the displacement of the mass and *dynamic simulations* predicted the resonant frequency of the devices. Finally, fitting the simulations with the theory developed, allowed us to verify the goodness of the model and

obtain geometrical parameters to complete it.

Chapter 5. Measurements

Measurements of the resonant frequency shifts of the devices when they are under a known acceleration. All the equipment and methods used are explained, to guide the reader through the tools and steps used to obtain the results.

Chapter 6. Discussion

The origin of the resonant frequency shift observed in the measurements is discussed. An origin different from the acceleration is proposed.

Chapter 7. Conclusions

Comparison between the theoretical model, the simulations and the measurements. The thesis finishes with insights and possible future work.

2 Devices

The devices studied during this thesis were created in the Department of Micro and Nanosystems of the KTH Royal Institute of Technology (Sweden). They are Accelerometers built with suspended graphene membranes that are fully clamped at their circumference and have attached silicon proof masses.

The devices were designed to measure accelerations by measuring the changes of electrical resistance of the graphene membrane.[I] The study was successful and published in *Nature Electronics* ([1] and [8]).

In our research, we re-use the same devices for a different purpose. The hypothesis to prove is that accelerations can be measured by monitoring the changes in the resonant frequency of the devices. The shifts in resonant frequency must be proportional to the applied external acceleration.

2.1 Accelerometers with graphene membrane

The accelerometers have a suspended silicon proof mass held by a double-layer graphene membrane, which is clamped at its entire circumference. They have variations in the attached mass and membrane dimensions to study how these parameters influence the measurements.

[I] The acceleration force acting on the proof mass causes a deflection of the mass. This causes a change of the strain on the suspended graphene membrane, resulting in a change of the electrical resistance because of the piezoresistivity of graphene.

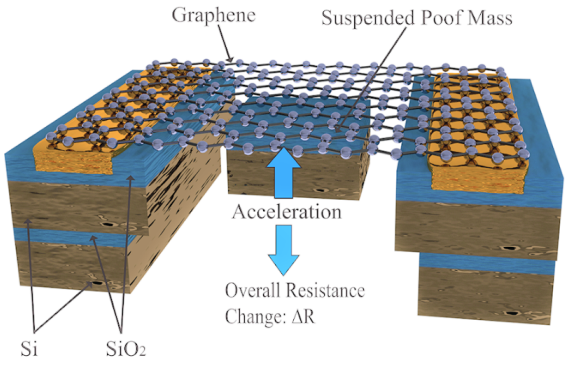

(a) Cross-sectional 3D illustration of a fully clamped graphene membrane with attached proof mass. The double-layer graphene membrane has 0.67 nm of thickness. Picture taken from [1]

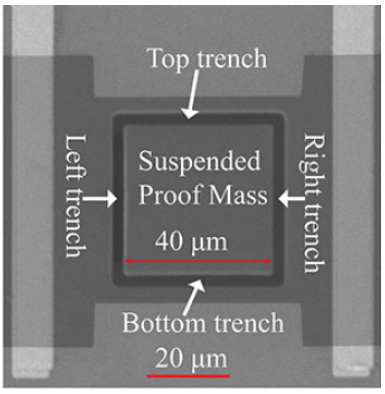

(b) Microscope image of a 40 μm mass accelerometer. The trench between mass and silicon is 3 μm, and the size of the mass can change.[1]

Figure 2.1 – Accelerometers made with a double-layer graphene membrane that is fully clamped and has a mass attached. In our research, we will study whether these devices are useful to measure accelerations studying the changes in the resonant frequency.

The accelerometer masses range from 10 μm to 100 μm of square area and 16.4 μm of height (this parameter is constant for all). The nomenclature to designate the accelerometers will be directly the mass side. For example, for the accelerometers that have masses of 40 μm x 40 μm x 16.4 μm, we will name them "40 μm".

The fabrication of these devices was not part of the research project. For that reason, to know more about the fabrication process we advise the reader to consult the original publication [1].

3 Analytical Model

The working principle of the accelerometers is based on the force created on the proof mass caused by the external acceleration. This force creates a displacement of the mass which results in a change of the membrane stress (tension) that holds the mass. The change in the tension directly affects the resonant frequency of the device.

Our purpose is to create a model that can predict and explain the variation in frequency due to a certain applied acceleration. Firstly, the device model needs to be simplified, while maintaining what is important.

Since the system is symmetric and the proof mass is rigid compared to the graphene membrane, the model can be simplified to a single graphene membrane with a centre point load (Figure 3.1). In that case, the effective length of the membrane equals two times the trench width. The membrane will always be considered squared of length (L), where (L/2) is the device's trench.

This approximation is valid as long as the real membrane area is considered when distributing the produced force (F). For that purpose, we will work with Pressure units.

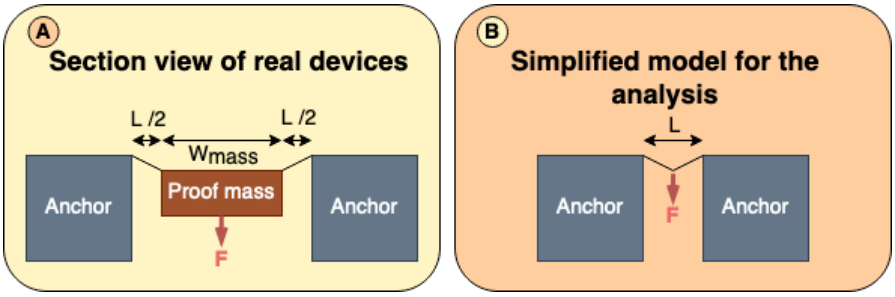

Figure 3.1 – Simplified model for the analytical study. In A): Transversal cut in the accelerometer. The mass is held by sections of the graphene membrane. In B): Simplified device model consisting of a graphene membrane with a centre point load. The membrane is squared with length equal to the double of the trench size.

3.1 Theoretical Resonant Frequency

Obtaining a complete theoretical model for the accelerometers can be highly algebraically complex. A better alternative is to use a more general solution for the load-deflection relation and use finite element simulations to verify the goodness of the expression and to determine values for the missing geometrical constants.

The general form for the load-deflection characteristic is the one seen in Equation 3.1, which is obtained from reference [6].

$$P = \left(C_{Tension}\left[\frac{\sigma_0 H}{L^2}\right] + C_{lin}\left[\frac{EH^3}{(1-\nu^2)L^4}\right]\right)Z + C_{nlin}\left[\frac{EH}{(1-\nu^2)L^4}\right]Z^3 \tag{3.1}$$

This equation relates the Pressure exerted over the membrane (P) with the membrane displacement (Z) through the membrane geometry: the thickness of the membrane (H), the length of membrane (twice the trench distance) (L). Other parameters involved are the built-in stress of the membrane (σ_0), the Poisson's ratio (ν) of graphene and Young's modulus (E). To adjust this model to the specific geometry of the accelerometers, we dispose of three variables: $C_{Tension}$ (multiplying the built-in tension of the membrane), C_{lin} (weighting the linear contribution) and C_{nlin} (taking into account the non-linear component).

The terms are re-arranged to express the formula in a linearized way:

$$P = \frac{C_{Tension}H}{L^2}\left(\sigma_0 + \frac{C_{lin}}{C_{Tension}}\left[\frac{EH^2}{(1-\nu^2)L^2}\right] + \frac{C_{nlin}}{C_{Tension}}\left[\frac{E}{(1-\nu^2)L^2}\right]Z^2\right)\cdot Z \tag{3.2}$$

Afterwards, the pressure is converted into force. For that, we use the Area of the membrane from the real accelerometers. This one is obtained geometrically, taking into account the parts of the membrane that are in the trenches.

$$P = \frac{F}{Area} \quad \text{and} \quad Area = (W_{mass}+L)^2 - W_{mass}^2 = 2W_{mass}\cdot L + L^2 \tag{3.3}$$

Here the width of the mass (W_{mass}) comes into play and will be inside the variable $Area$.

$$F = Area\cdot\frac{C_{Tension}H}{L^2}\left(\sigma_0 + \frac{C_{lin}}{C_{Tension}}\left[\frac{EH^2}{(1-\nu^2)L^2}\right] + \frac{C_{nlin}}{C_{Tension}}\left[\frac{E}{(1-\nu^2)L^2}\right]Z^2\right)\cdot Z \tag{3.4}$$

Next, we calculate the stiffness, which for a nonlinear resonator is obtained through the displacement derivative of the Force equation 3.4. Reference [9].

$$k = \frac{dF}{dz} = Area\cdot\frac{C_{Tension}H}{L^2}\left(\sigma_0 + \frac{C_{lin}}{C_{Tension}}\left[\frac{EH^2}{(1-\nu^2)L^2}\right] + \frac{3\cdot C_{nlin}}{C_{Tension}}\left[\frac{E}{(1-\nu^2)L^2}\right]Z^2\right) \tag{3.5}$$

Afterwards, the natural frequency (resonant frequency) of the device can be obtained with the relation: $k = (2\pi f_R)^2 m$

$$Area \cdot \frac{C_{Tension} H}{L^2}\left(\sigma_0 + \frac{C_{lin}}{C_{Tension}}\left[\frac{EH^2}{(1-\nu^2)L^2}\right] + \frac{3 \cdot C_{nlin}}{C_{Tension}}\left[\frac{E}{(1-\nu^2)L^2}\right] Z^2\right) = (2\pi f_R)^2 m \quad (3.6)$$

$$f_R = \frac{1}{2\pi}\sqrt{\frac{Area \cdot C_{Tension} H}{mL^2}\left[\sigma_0 + \frac{C_{lin}}{C_{Tension}}\frac{EH^2}{(1-\nu^2)L^2} + \frac{3 \cdot C_{nlin}}{C_{Tension}}\frac{E}{(1-\nu^2)L^2} Z^2\right]} \quad (3.7)$$

We observe that the frequency depends on the displacement. Which, at the same time, could be obtained from the expression $Z = F/k$ (Equation 3.4). This means that every time we want to solve the frequency equation 3.7, the displacement needs to be solved first by employing a root-finding algorithm. For this case, the Newton-Raphson method is used.

$$Z = \frac{m \cdot a}{Area \cdot \frac{C_{Tension} H}{L^2}\left[\sigma_0 + \frac{C_{lin}}{C_{Tension}}\left[\frac{EH^2}{(1-\nu^2)L^2}\right] + \frac{C_{nlin}}{C_{Tension}}\left[\frac{E}{(1-\nu^2)L^2}\right] Z^2\right]} \rightarrow \text{Solved using Newton-Raphson} \quad (3.8)$$

The *Responsivity* ($\mathscr{R}$) of our devices is the parameter that tells us the goodness of the device acting as an acceleration sensor. In our case, it is defined as the shift in resonant frequency divided by the acceleration applied. This figure is divided by the resonance frequency to only have acceleration units. Our measurements always have the Earth's gravity bias, for that reason, the responsivity is evaluated for an acceleration equal to the Earth's gravity (g).

$$\mathscr{R} = \frac{1}{f_R(g)} \cdot \left.\frac{\partial f}{\partial a}\right|_g = \frac{1}{f_R(g)} \frac{f_R(g + \Delta a) - f_R(g)}{\Delta a} \quad (3.9)$$

The use of the Responsivity parameter allows us to observe how the resonant frequency of the device is modified by an external acceleration acting on the device.

3.2 Simplified Responsivity expression

The Responsivity is always calculated using the Root-finding algorithm, which makes it possible to resolve the nonlinear equation. However, to be able to create an intuition on how the Responsivity depends on the other parameters, a simplified expression is needed.

The approximation is to consider large built-in membrane tensions, to make some simplifications in the Displacement denominator, as seen in 3.10.

$$\begin{cases} f_R = \frac{1}{2\pi}\sqrt{\frac{Area\cdot C_{Tension}H}{mL^2}\left[\sigma_0 + \frac{C_{lin}}{C_{Tension}}\frac{EH^2}{(1-\nu^2)L^2} + \frac{3\cdot C_{nlin}}{C_{Tension}}\frac{E}{(1-\nu^2)L^2}Z^2\right]} \\ Z = \frac{m\cdot a}{Area\cdot\frac{C_{Tension}H}{L^2}\left[\sigma_0 + \frac{C_{lin}}{C_{Tension}}\left[\frac{EH^2}{(1-\nu^2)L^2}\right] + \frac{C_{nlin}}{C_{Tension}}\left[\frac{E}{(1-\nu^2)L^2}\right]Z^2\right]} \end{cases}$$

$$\mathscr{R} \approx \frac{3C_{nlin}EL^4m^2g}{Area^2C_{lin}C_{tension}^2EH^4\sigma_0^2 + Area^2C_{tension}^3H^2L^2\sigma_0^3(1-\nu^2) + 3C_{nlin}EL^4m^2g^2} \tag{3.10}$$

Thanks to the simplified formula for the responsivity, we observe that for increasing values of σ_0, the responsivity decays to zero ($R \propto \sigma_0^{-3}$). So we observe higher responsivity whenever the built-in stress in the devices is low.

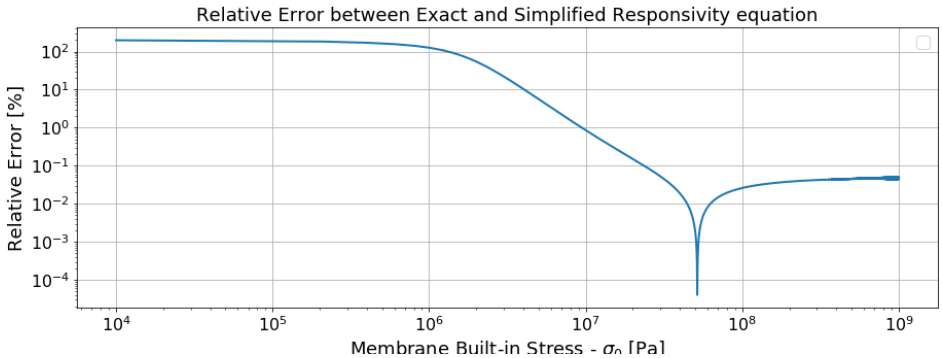

Figure 3.2 – Relative error between exact responsivity from the root-finding algorithm and the simplified analytical expression 3.10. We can observe that the formula is only accurate for large membrane built-in stresses. The simplified equation will not be used in the fittings, but the expression is useful to visually evaluate the parameter dependencies.

4 Finite Element Simulations

Simulations are of key importance to obtain a complete theoretical model for the accelerometers. As seen in Section 3, the analytical method depends on some variables ($C_{tension}$, C_{lin} and C_{nlin}) that need to be adjusted with simulations.

The finite element analysis simulations are performed in COMSOL and the data output analysed with Python.

4.1 Graphene membrane devices simulations

To avoid not-on-axis movements an axisymmetric simulation is performed. That means that the model is designed in 2D and then using a rotation the 3D is built. With this procedure it is impossible to simulate the proof mass as a cuboid, so we translate the same properties into a cylindrical mass. The translation keeps the volume (and therefore mass) constant.

$$V_{Cuboid} = V_{Cylinder}$$

$$W_{mass}^2 \cdot height = \pi R_{mass}^2 \cdot height$$

$$R_{mass} = \frac{W_{mass}}{\sqrt{\pi}}$$

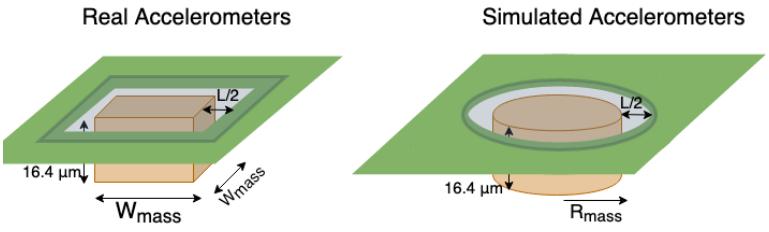

Figure 4.1 – Real accelerometers on the left and simulated model on the right. The mass size is translated into a cylindrical shape preserving the volume and the trench length.

In the simulations, the material properties of the original elements are respected: the mass is made out of silicon (density = 2330 kg/m^3) and the membrane are made of graphene ($\nu = 0.25$, $E = 0.22\ TPa$). The whole accelerometer is simulated using *solid mechanics* and initial stress is implemented in the membrane (acting like the built-in stress σ_0).

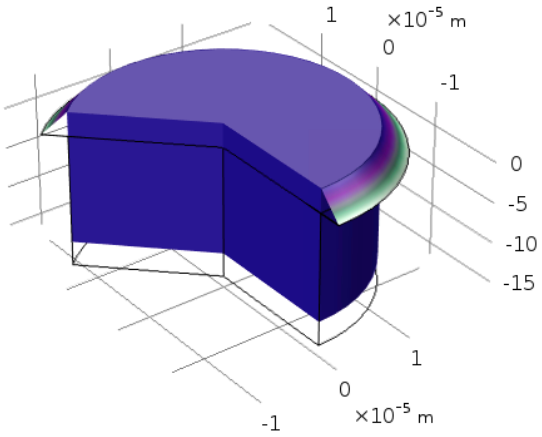

Figure 4.2 – Simulation of the graphene membrane accelerometer. The geometry is built through axial symmetry from a 2D model to avoid not-on-axis movements. The end of the graphene membrane is anchored with a fixed constraint, avoiding a place where the meshing would fail. With all these simplifications we achieve convergence of the simulations.

As seen in Figure 4.2, the silicon anchor is replaced by a fixed constraint in the membrane end. These simplifications are needed to have a good convergence of the solutions. This is the major difficulty for the simulations, due to the large ratio between length and thickness of the membrane (L = $3 \cdot 10^{-6}$ m and H = $0.67 \cdot 10^{-9}$ m) which has a ratio of 4500. This means that the mesh has to be carefully chosen to be able to solve the simulation. A quadrilateral mesh is created with a minimum element size of 10 pm and a maximum of 3.6 μm.

4.1.1 Static Simulation: Mass displacement study

The static simulations obtain the deflection of the mass due to the external acceleration. As we always operate with the Earth's gravity bias, simulations shown in Figure 4.3 are under 1 g of acceleration. The static displacement of the mass is simulated for different built-in membrane stresses and different mass sizes.

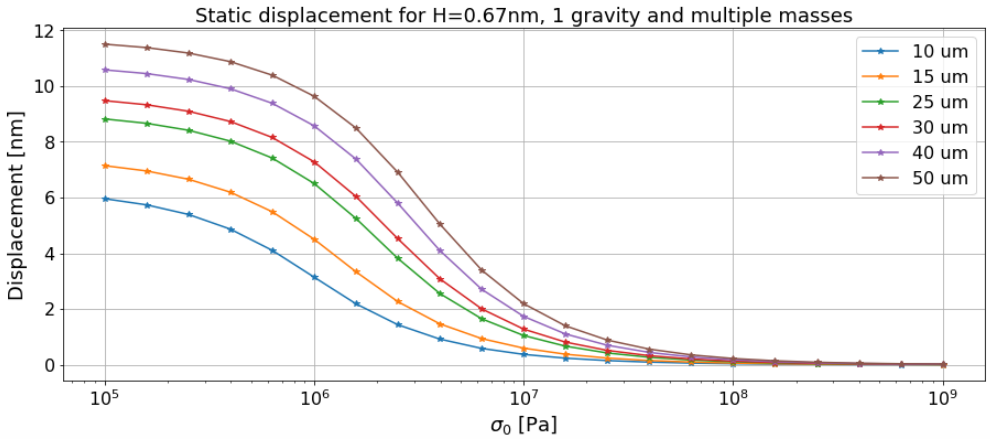

Figure 4.3 – Displacement of the mass due to the external acceleration (only Earth's gravity in this case) for the different mass widths. The figure shows how the static displacement of the mass is reduced with the increase of the membrane stress. The limit is when the membrane is so stressed that regardless of the external acceleration, the mass stays at the same height as the silicon chip (zero displacement).

From Figure 4.3 we observe how the increase of the membrane tension reduces the displacement of the membrane when the stress is higher than 0.1MPa. Below that stress, the displacement is maintained constant.

To relate the static simulation with the devices we need to perform dynamic simulations. These will create the link between the resonant frequency of the devices with the membrane built-in stress.

4.1.2 Dynamic Simulation: Resonant frequency study

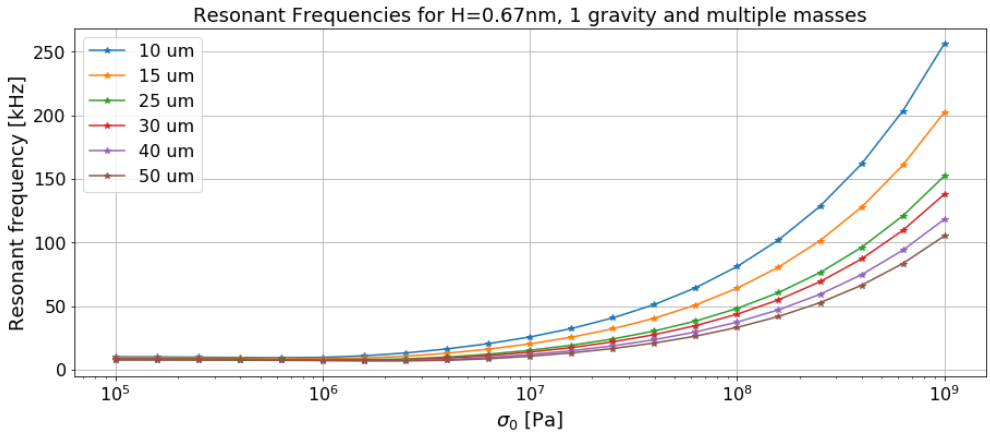

Figure 4.4 – Study of the resonant frequency of membrane accelerometers with different proof masses. The applied acceleration is equal to the gravity. This study gives the opportunity to directly know the membrane stress knowing the resonant frequency of the devices.

The dynamic study of our devices allows to simulate the resonant frequency depending on the built-in stress of the membranes (σ_0). The simulation is performed for the different mass sizes of the real accelerometers (10 μm to 50 μm of width).

4.1.3 Dynamic Simulation: Effect of the external acceleration

In this study, we set a constant mass size (30 μm) and we perform dynamic simulations varying the external acceleration. Here, we can see the magnitude of the resonant frequency shifts due to the external acceleration. In Figure 4.5 some extreme cases are shown to see the effects: No applied gravity, Earth's gravity and 10 times Earth's gravity.

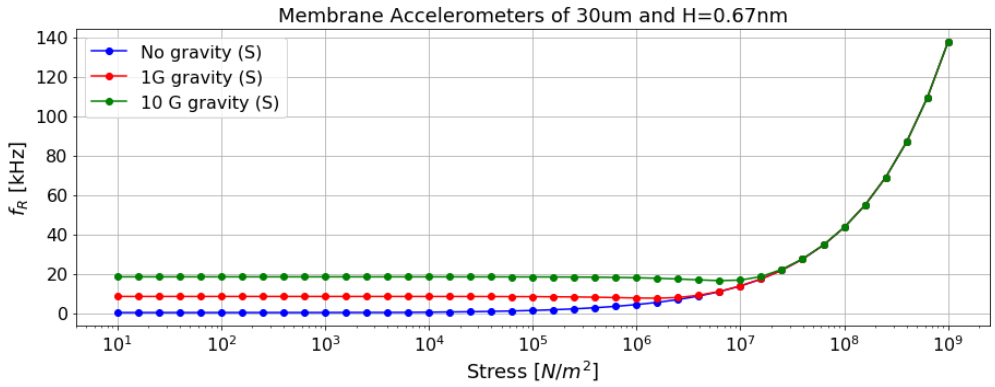

Figure 4.5 – Resonant frequency study for a device with 30μm width mass under three different external accelerations. As expected, the presence of an external force increases the membrane stress and increases the resonant frequency. The effect is predominant when the built-in membrane stress is low. With an increasing value of the membrane stress, the change in acceleration is not able to change the resonant frequency.

From Figure 4.5, the increase in external acceleration produces an increase in the membrane stress, which is translated into a higher resonant frequency. When the built-in stress is high enough, the frequencies converge, regardless of the external acceleration. These simulations give us the idea that the built-in stress of the graphene membranes will play an important role in the *Responsivity* of the devices, as predicted in Chapter 3.

4.2 Nonlinearities

The theoretical model developed in Section 3.1 is nonlinear, as the force depends on the third power of the displacement. Before fitting the results of the previous section with the analytical model, we characterise the importance of the nonlinearities in our devices.

The first procedure to study the nonlinearities is based on the differences of the membrane profiles for *static* and *dynamic* studies. If the membrane profile is identical, the nonlinearity is negligible, meaning that the Elastic Constant in static and dynamic are similar.

This method allows us to see for which parameters the nonlinear term has a bigger influence. The used variable is the % *Error* between the profile of the membrane during the Static and the Modal study.

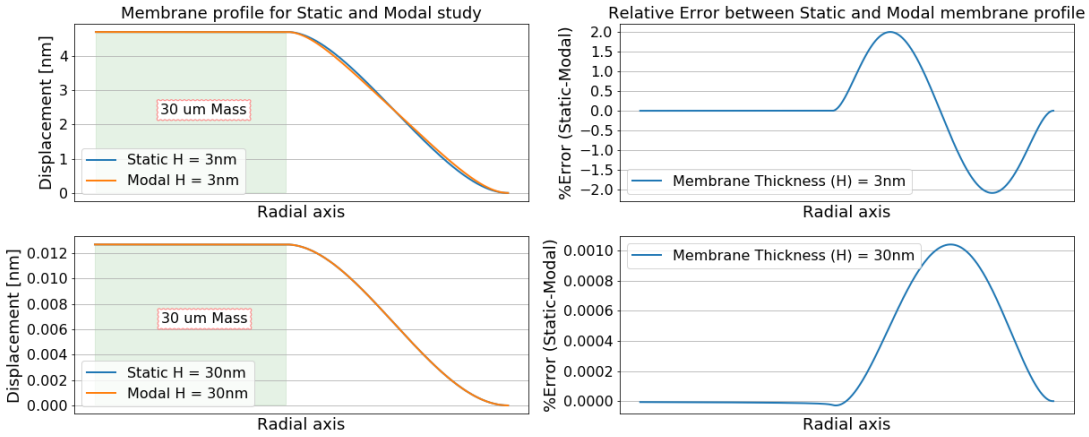

Figure 4.6 – The difference between the membrane profiles during Static and Modal studies tells whether the device is in a nonlinear regime. The bigger the difference between the profiles, the bigger the importance of the nonlinear terms. In this Figure, the comparison between membrane profiles in static and dynamic simulations for two membrane thicknesses is shown. When the membrane thickness is 3 nm (**Top**), the differences between the profiles are larger than the case of 30 nm thickness (**Down**). On the left, we can see the membrane profiles during Static and Modal studies and on the right the % of error between the profiles. These two cases show us that nonlinearities are larger when the thickness is 3 nm than 30 nm.

To study the differences seen in Figure 4.6 in more detail, the relative error is computed over a range of membrane thickness values. The Figure 4.7 shows the result for an accelerometer of 30 μm mass, under 1 gravity and with no built-in tension in the membrane.

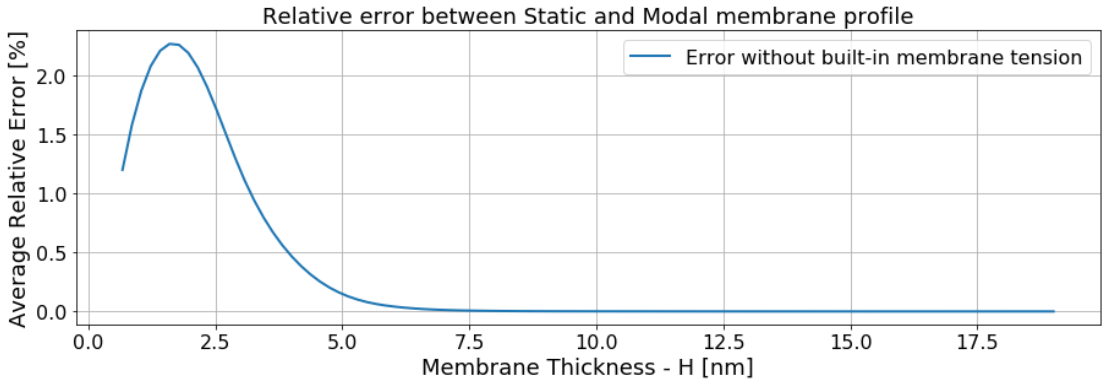

Figure 4.7 – Error between membrane profiles in static and modal simulations with no built-in tension and for different values of the graphene thickness (H). We observe that for membranes thicker than 6 nm the nonlinearity is totally negligible for every built-in tension.

The next step is to see how the nonlinearities vary with the built-in stress of the membrane. The study shown in Figure 4.8 is performed for several mass widths under gravitational acceleration. This time, the membrane thickness is set to the graphene one (0.67 nm).

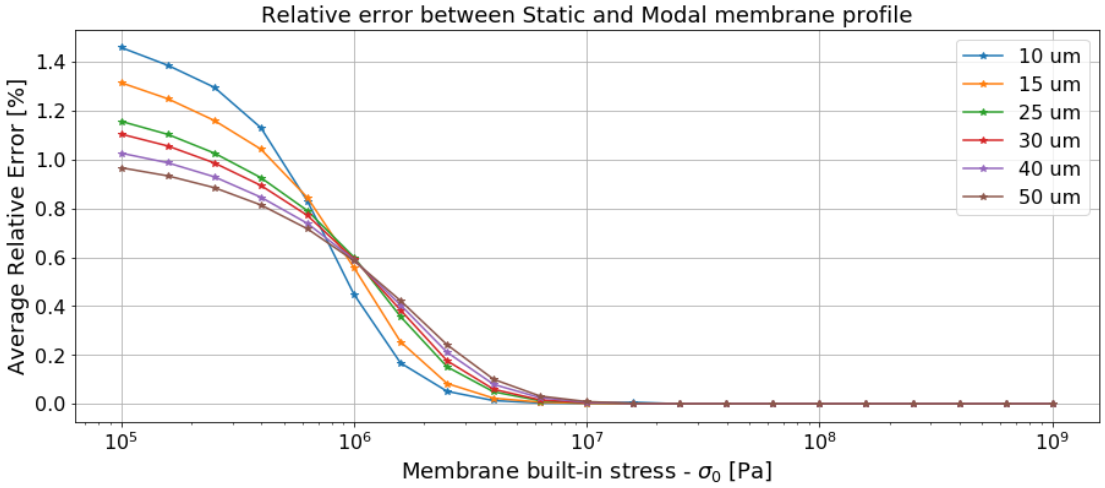

Figure 4.8 – Error between membrane profiles in static and modal simulations for different membrane stresses and different proof masses. The study is performed with a membrane thickness of 0.67 nm and under Earth's gravity acceleration. The results show that nonlinearities start to be negligible after 10 MPa.

4.2.1 Nonlinearity related to the accelerometer geometry

The next study researches what is the implication of the membrane thickness (H) and trench length (L) in the creation of nonlinear behaviour. Both variables are swept to see if a relation between H and L exists in terms of nonlinearities.

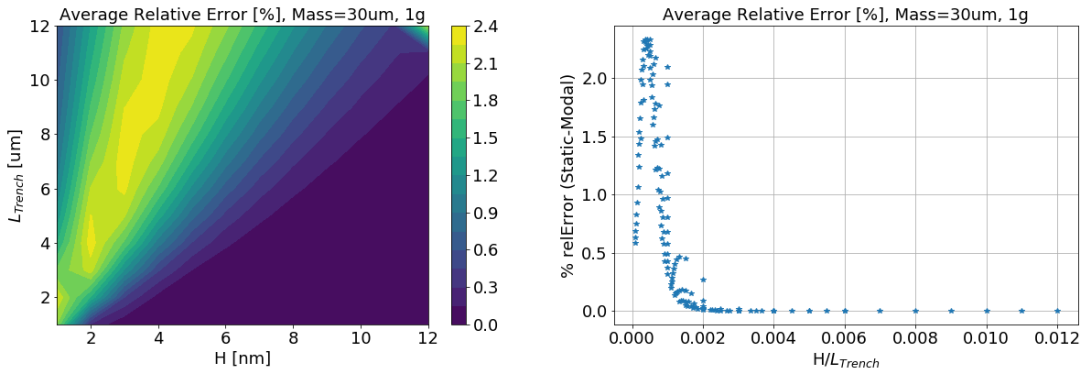

Figure 4.9 – Left: Nonlinearity study with sweeps in H and L. **Right:** The simulations have been sorted by the ratio H/L. We observe that the ratio of H and L decides if the device operates in nonlinearity. For this specific case, with no built-in tension, the Length of the trench must be 500 times larger than the thickness of the graphene to be working in the linear region.

Figure 4.9 shows the effect of the membrane thickness and length in determining whether the system is in linear region. The system is more nonlinear whenever the ratio between the membrane thickness and its trench length is smaller. For the case when the membrane tension is small, the trench must be 500 times larger than the thickness to be in the linear region.

4.3 Fitting the model

In this section, the theoretical model developed in Section 3.1, is fitted to the simulations to obtain the values of the parameters $C_{tension}$, C_{lin} and C_{nlin}.

$$Z = \frac{m \cdot a}{Area \cdot \frac{C_{Tension} H}{L^2}\left[\sigma_0 + \frac{C_{lin}}{C_{Tension}}\left[\frac{EH^2}{(1-\nu^2)L^2}\right] + \frac{C_{nlin}}{C_{Tension}}\left[\frac{E}{(1-\nu^2)L^2}\right]Z^2\right]} \tag{4.1}$$

$$f_o = \frac{1}{2\pi}\sqrt{\frac{Area \cdot C_{Tension} H}{mL^2}\left[\sigma_0 + \frac{C_{lin}}{C_{Tension}}\frac{EH^2}{(1-\nu^2)L^2} + \frac{3 \cdot C_{nlin}}{C_{Tension}}\frac{E}{(1-\nu^2)L^2}Z^2\right]} \tag{4.2}$$

In Section 4.2 we conclude that the nonlinear and linear behaviour has its boundary around a membrane tension of 10 MPa (when using graphene geometrical parameters). We need to consider this when fitting the data. The linear term is best fitted in the linear region and has a higher error in the nonlinear part. The opposite happens for the nonlinear coefficient.

To be sure that the model is adjusted in the linear and nonlinear regimes, the membrane thickness is varied. Static simulations are performed, obtaining the displacement for an accelerometer of 30 μm mass without membrane tension. The dynamic simulations obtain

the resonant frequencies under the same circumstances.

The results of the fittings for the linear and nonlinear coefficients can be seen in Figures 4.10 and 4.11. We observe that the linear coefficient C_{lin} are well fitted where the linear behaviour dominates. On the other side, the nonlinear coefficient C_{nlin} can be well fitted in the nonlinear region. In these simulations, the coefficient $C_{Tension}$ cannot be obtained because the membrane tension is set to zero.

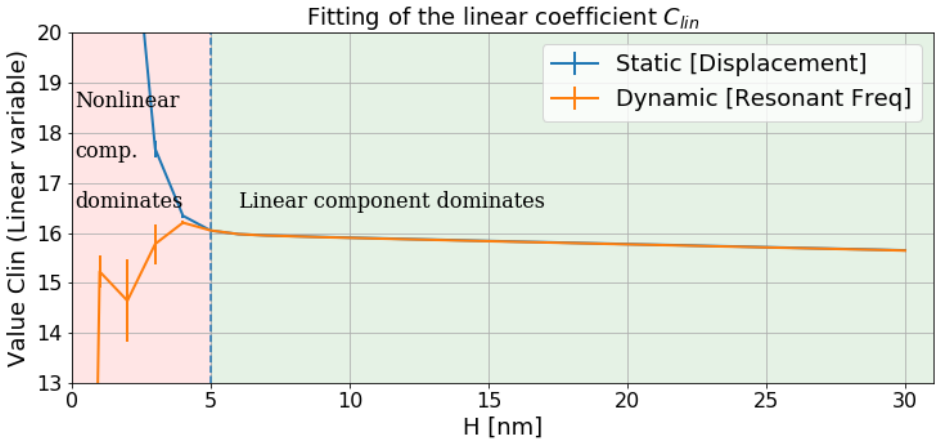

Figure 4.10 – Fitting the model to obtain the linear coefficient C_{lin}. The static and dynamic simulations fitted with the theoretical model give the same values in the linear region. In the nonlinear region, the linear coefficient is not important and takes an arbitrarily large value. From this study we obtain the value of the linear coefficient to be around 15.9 (More simulations are performed to increase certainty).

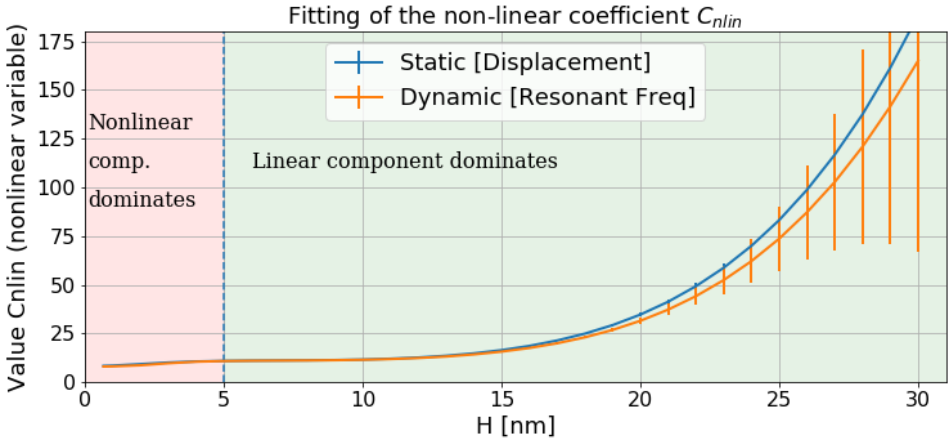

Figure 4.11 – Fitting of the nonlinear coefficient C_{nlin}. The static and dynamic simulations give the same values in the nonlinear region. In the linear region, the nonlinear coefficient is not important and takes an arbitrarily large value. From this study we obtain the value of the nonlinear coefficient is 8.0.

Now we need to obtain the value for $C_{Tension}$ and double-check the value of the others coefficients. For that purpose, static and dynamic simulations are performed for different stresses.

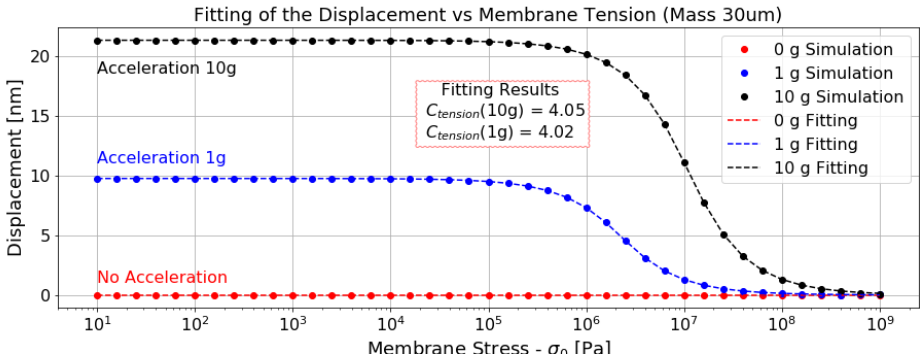

Figure 4.12 – Fitting of the displacement vs membrane tension for an accelerometer with 30μm mass. From this fitting, the value for $C_{tension}$ is seen to be 4.05 (for an external acceleration of 1g) and 4.02 (for an external acceleration of 10g).

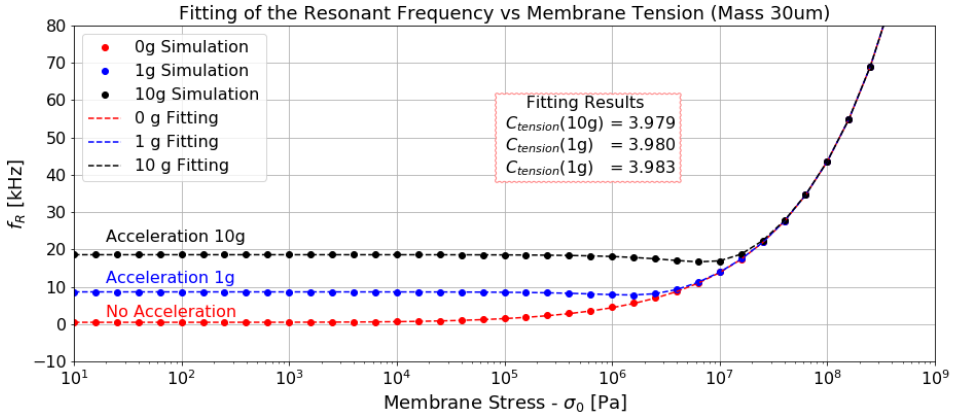

Figure 4.13 – Fitting of the resonant frequency when varying the membrane tension for an accelerometer with 30μm mass. From this fitting, the value for $C_{tension}$ is seen to be 3.983 (without external acceleration), 3.980 (for an external acceleration of 1g) and 3.979 (for an external acceleration of 10g).

The next study is performed without membrane stress, performing a sweep in gravity. In these conditions, the device works in the nonlinear region. Only the nonlinear coefficient C_{nlin} can be extracted from this study.

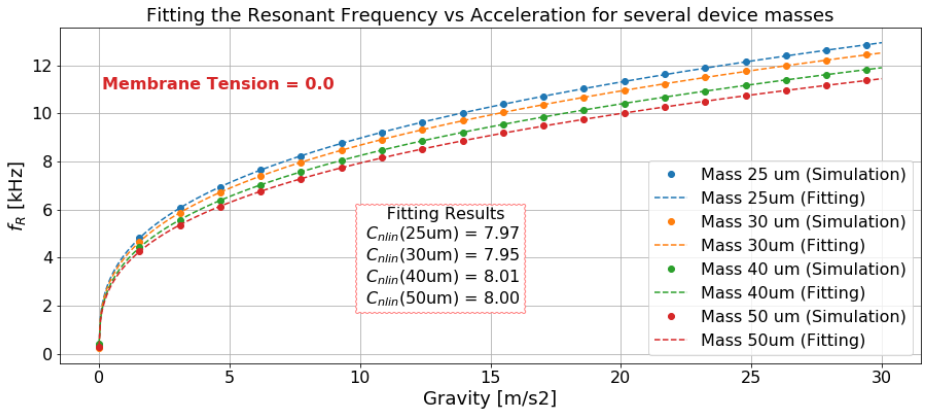

Figure 4.14 – Fitting of the resonant frequency when varying the external acceleration. Study performed for zero built-in stress and for different mass sizes. All the fittings give a similar value for C_{nlin} around 8.0.

Gathering the data of all the fittings, we conclude that the values for the geometric constants of our devices are:

$C_{Tension}$	C_{lin}	C_{nlin}
4.002 ± 0.028	15.94 ± 0.036	7.9825 ± 0.024

4.3.1 Responsivity study

At this moment, we dispose of a complete theoretical model with which we can assess the Responsivity of our devices. Thanks to this study, knowing the resonant frequency of the devices (measured in Chapter 5. Measurements) allows us to predict the Responsivity and the stress of the membrane. The Figure 4.15 joins the most important parameter of our devices: the resonant frequency and the Responsivity, related by the Membrane built-in stress. The resonant frequency determines the bandwidth of the accelerometer and the responsivity the possibility of accurately measuring accelerations.

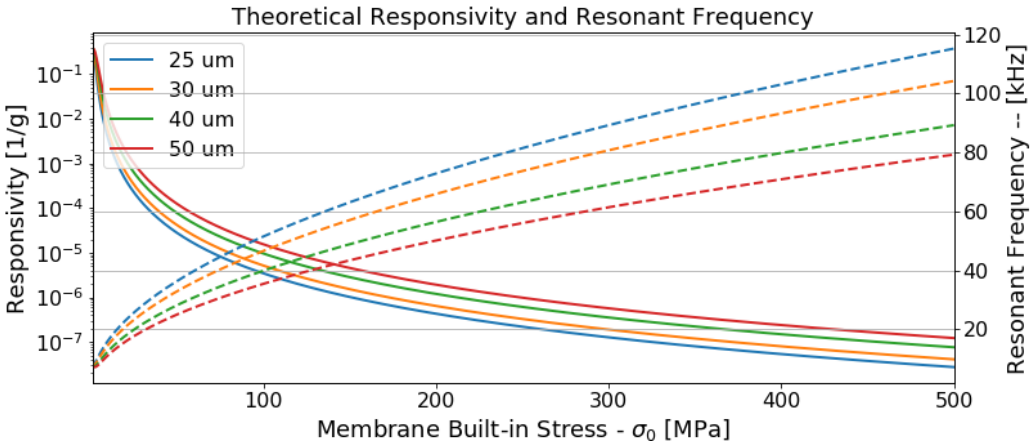

Figure 4.15 – Theoretical Responsivity and Resonant Frequency depending on the Membrane tension. Knowing the Resonant Frequency of one accelerometer we can extract the membrane tension and the responsivity directly from this plot.

The Figure 4.15 is useful to predict which would be the Responsivity and Membrane Built-in Tension of the devices knowing their Resonant Frequency. From a theoretical standpoint, we expect low responsivities for our accelerometers.

Responsivity comparison with nonresonant accelerometers

An important question to answer is whether these accelerometers are better than the current nonresonant accelerometer technology. To compare both technologies, we plot the minimum acceleration detectable against their resonant frequency.

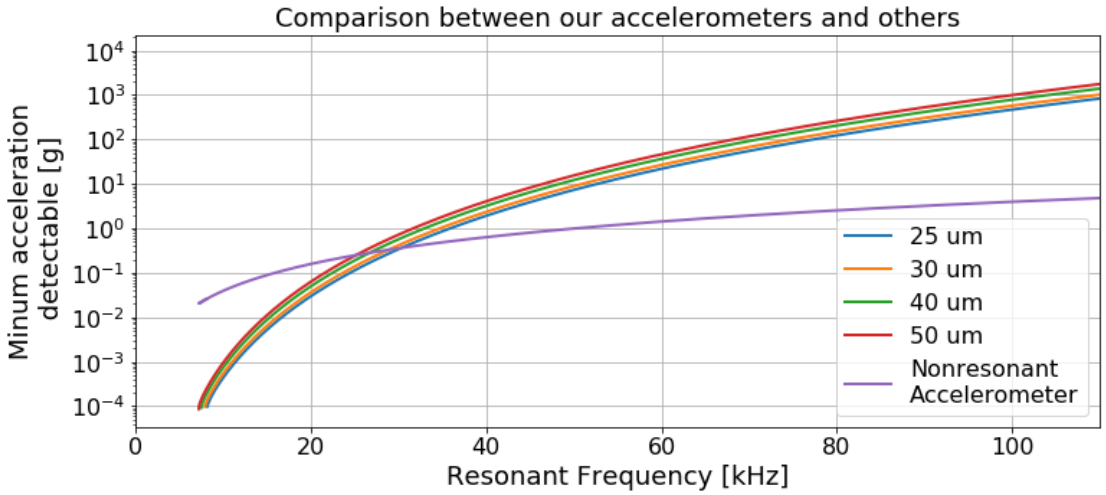

Figure 4.16 – Comparison between our accelerometers and typical nonresonant accelerometer. This comparison is made for typical parameters (Allan deviation of 10 ppm for our devices and displacements of 10 pm for the nonresonant accelerometers). For low resonant frequency we find that our accelerometers have better sensitivity, for larger frequencies the average nonresonant accelerometer performs better.

From Figure 4.16 we can observe that, based on the theory, our accelerometers perform better for resonant frequencies under 40 kHz. On the other hand, for larger resonant frequencies, the average nonresonant accelerometer can detect lower accelerations.

5 Measurements

In chapters 3 and 4, the theoretical analysis and the respective simulations for the graphene accelerometers were shown. The next step is to verify them with measurements on the actual devices. We are interested in the *Responsivity* of the devices, which for us, is understood as: "How much the resonant frequency is shifted due to an acceleration acting on the device". This magnitude is then normalized by the resonant frequency to only depend on acceleration units.

$$\mathscr{R} = \frac{1}{f_R(g)} \cdot \left.\frac{\partial f_R}{\partial a}\right|_g \tag{5.1}$$

For that purpose, the resonant frequency of each accelerometer must be measured, while the acceleration is applied. The best way to do this is by using a Laser Doppler Vibrometer and a piezo-shaker to excite the resonance of the device and produce accelerations. Everything is going to be explained step by step.

5.1 Laser Doppler Vibrometer (LDV)

The Laser Doppler Vibrometry (LDV) is a method that allows the measuring of displacements (resolutions down to 0.1 pm) and velocities (up to 25 m/s). Additionally, it enables to measure up to very large frequency ranges (from DC to 24 MHz) and the measurements can be performed independently of the measuring distance.

The working principle relies on the Doppler Effect produced in the laser that is pointed at the Device Under Test (DUT). Due to the movement of the DUT, the impinging light is reflected with a shift in frequency. This light merges with a reference from the laser and is sent to the detector (see Figure 5.1). The interference between the two beams can be constructive or destructive, light or dark patterns are generated. To go from the light to dark cycle on the detector means that the object displacement has been half of the laser wavelength (316 nm).

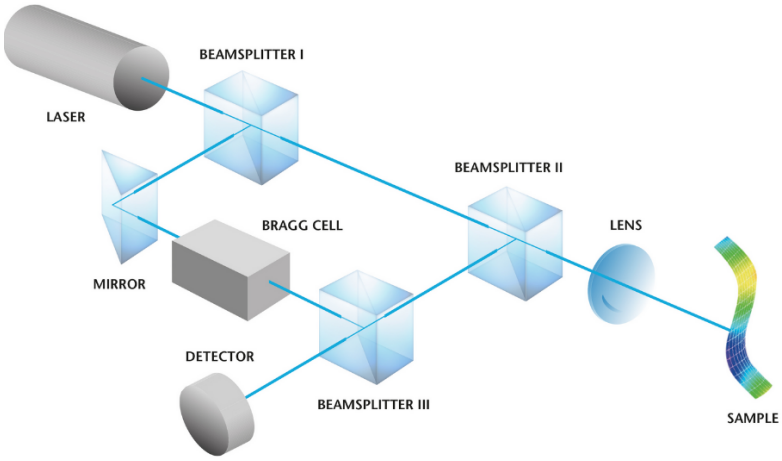

Figure 5.1 – The Laser Doppler Vibrometry is based on an interferometer. The Helium-Neon laser is split to obtain a reference and a measuring beam, which sense the movements of the sample. Both are combined into a detector and from their doppler shift the velocity and displacement of the sample are obtained.

5.2 Complete Set-up

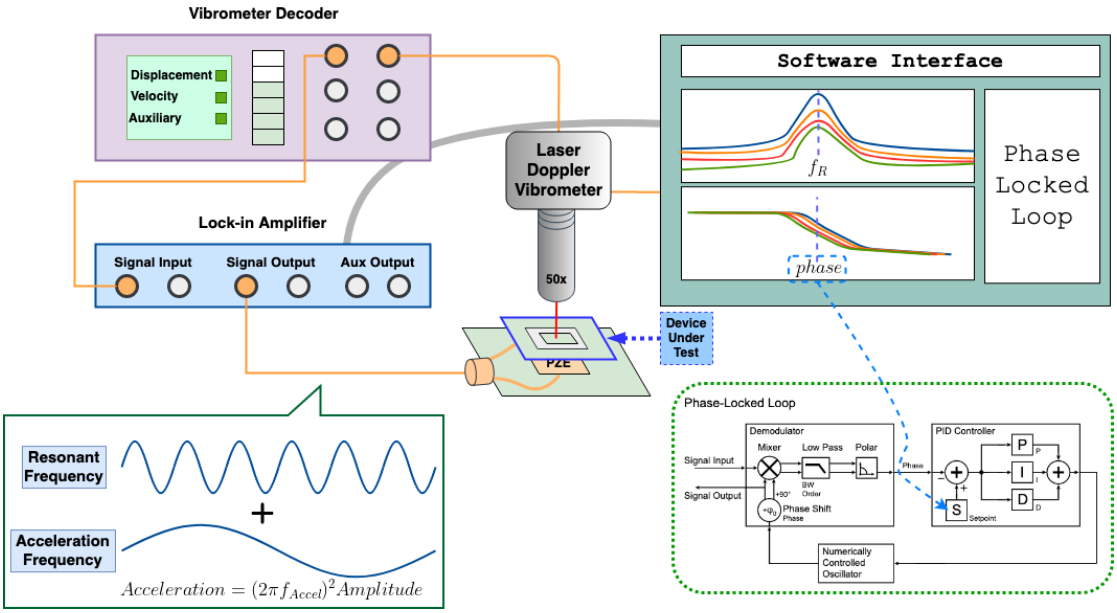

Figure 5.2 – Complete set-up to measure displacements and velocities from the Device Under Test (DUT). It is based on a Laser Doppler Vibrometer, a Vibrometer Decoder and a Lock-in amplifier. The goal is to excite the resonance of the DUT and to add an acceleration signal while measuring the resonant frequency changes.

As seen in Figure 5.2, the Laser Doppler Vibrometer is pointing at the device under test. This one lies over a piezo-shaker, which is a piezoelectric element that converts a given input

signal into vibrations in the Z-axis. With it, the resonant frequency of the accelerometer is excited. Simultaneously, a lower frequency signal which creates accelerations is introduced. The LDV signal is sent to the Vibrometer Decoder which converts it into a Displacement or Velocity measurement. This output is then read by the Lock-in amplifier and displayed in the computer.

To better understand how the measurements are taken, the next sections explain the procedure followed.

5.2.1 Measuring the Thermomechanical Noise

The thermomechanical study helps to find the resonant frequency of the device. We read the output of the LDV without any actuation of the piezo-shaker. Then, the data is digitally transformed into the frequency domain and the resonance can be distinguished. Additionally, the noise floor of the measurement can be known in Power Spectral Density units $[V^2/Hz]$.

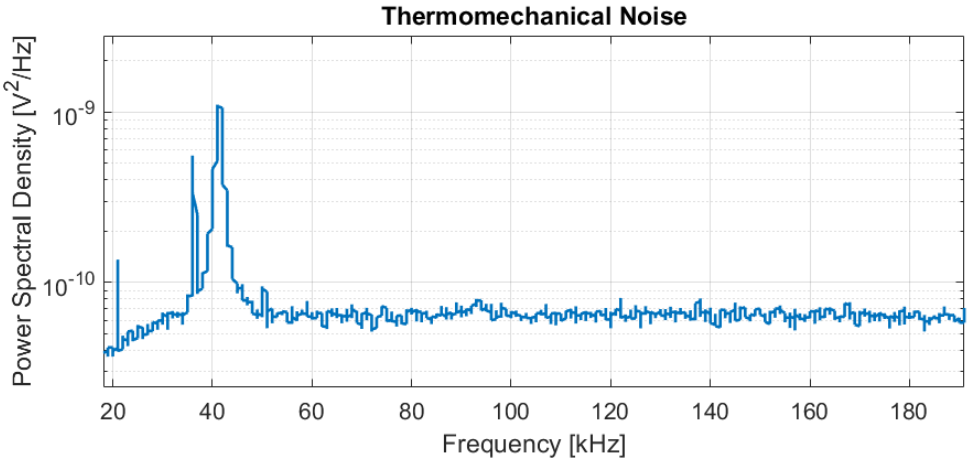

Figure 5.3 – Thermomechanical Noise measurement of a membrane graphene accelerometer (E6). This kind of measurements read the signal of the laser without the actuation of the piezo-shaker. Possible resonances of the devices can be seen and the thermomechanical noise can be known.

5.2.2 Sweep in Frequency

Once the possible resonant frequency is determined, the next step is to perform a sweep in frequency for different driving voltages of the piezo-shaker. In Figure 5.4 the resonance is identified and with the increase of the driving voltage, a linear increase in the amplitude is observed.

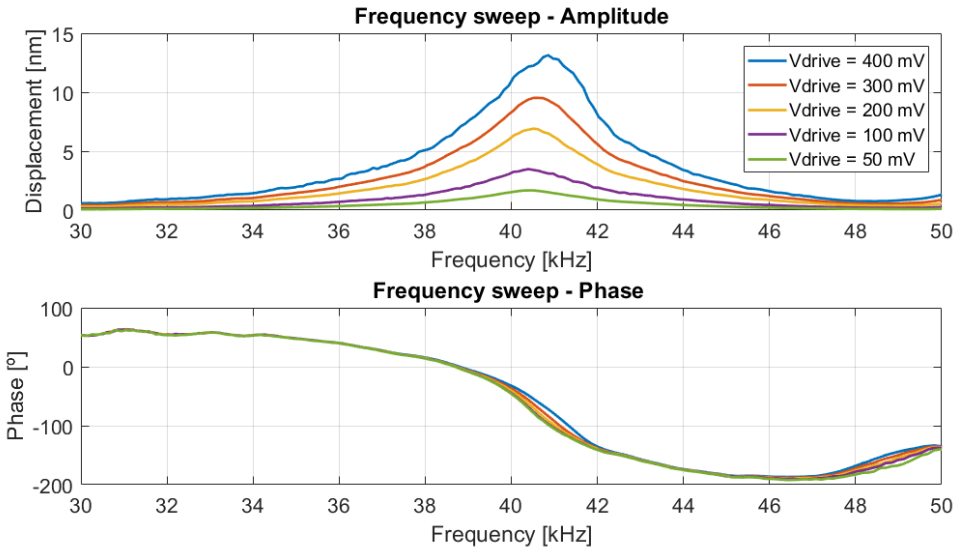

Figure 5.4 – Frequency sweep performed with the piezo-shaker attached to the device. This measurement allows for identifying the resonances. The change in driving voltage allows us to see a linear increase of the displacement of the proof mass oscillating at the resonant frequency.

5.2.3 Atomic Force Microscope Measurements

Atomic Force Microscope (AFM) measurements were performed to obtain the elastic constant and stresses of the graphene membrane. The AFM measurements allow us to input a force into the device and measure the displacement produced in the mass. The force is made with a tip attached to a cantilever, which makes contact with the object to measure. The slope between the Force and the Displacement will give us the Elastic constant ($F = k \cdot Z$). Moreover, we can extract information when the tip is increasing the force into the mass (Forward) and also when it is decreasing it (Backwards).

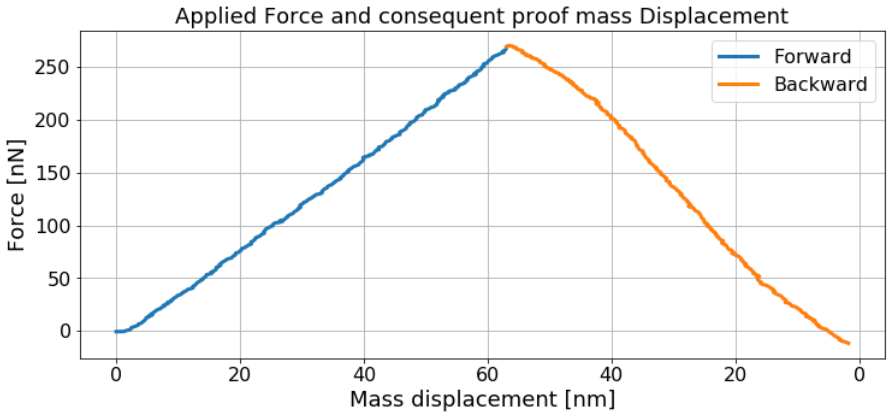

Figure 5.5 – AFM measurement where a force is applied over the proof mass of device D8 (25 μm, 168 kHz). This causes a deflection of the mass that depends on the *elastic constant*. From every AFM measurement the forward movement (while increasing the force on the mass) and backward movement (while decreasing the force) is recorded.

The devices are measured in ambient conditions using the *Tapping mode*. In this mode, the cantilever is oscillating near its resonance frequency and produces intermittent contacts with the sample surface. This allows us to have peak forces applied much higher than in contact mode, but with less damage done to the surface and the tip.

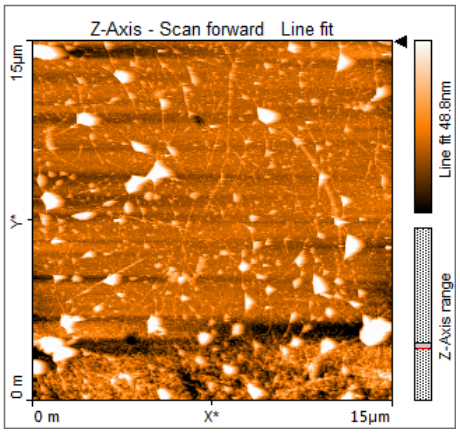

(a) AFM picture of the area studied (Device E6). We can observe that the graphene has PMMA residues, due to the graphene transfer process. [12]

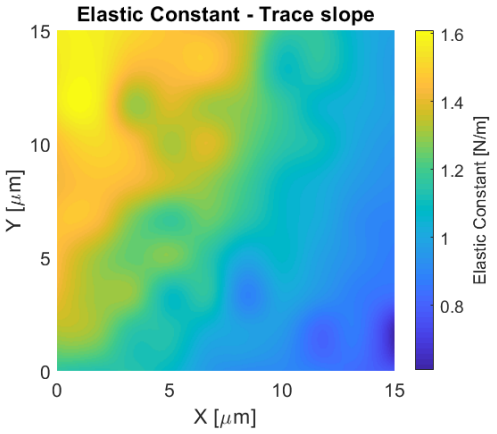

(b) Elastic Constant study performed in the area shown in a). We observe that half of the element has an elastic constant which is the double of the other side.

Figure 5.6 – **Left**: Topographical image of the E6 device. **Right**: Analysed AFM data to extract the elastic constant of 100 different positions on the same device.

This result in Figure 5.6 shows two different regions, one with a higher elastic constant than the other. The same conclusion are obtained from the measurements taken with the Digital

Holographic Microscope (DHM) [I].

The movement of the same device (E6, 30 μm and 40kHz) at resonant frequency is seen to be asymmetrical. The DHM allows the video recording of the device movement. Data over one period is converted in several profiles shown in Figure 5.7.

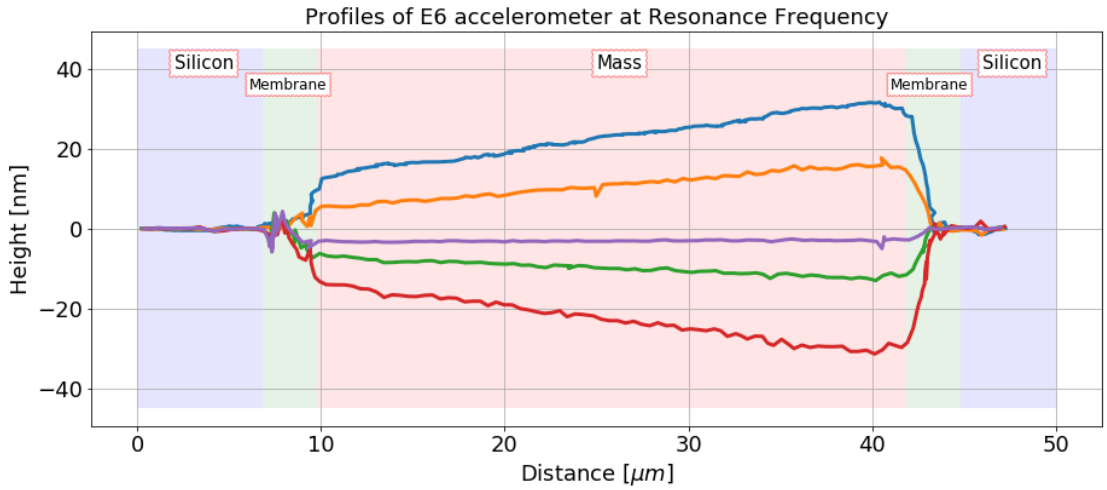

Figure 5.7 – Horizontal cut in E6 device to see the mass movement for different moments over its period at resonant frequency. We can observe that the movement is not symmetric, coinciding with the predictions from the AFM measurements. This measurements were taken with the Digital Holographic Microscope.

The same measurements were taken in other devices, with different results. That is the case of the E8 (30 μm, 112 kHz) device, where the AFM elastic constant study showed a much more homogeneous value in the studied area (Figure 5.8)

[I] The Digital Holographic Microscope is an instrument which allows the measuring of the reflected wavefront information originated from the object as a hologram. Using a computer algorithm, amplitude and phase information are obtained, enabling the reconstruction of movements in Z-axis. DHM allows measuring vertical ranges from nanometers to hundreds of microns with sub-nanometric vertical resolution. More information: www.lynceetec.com

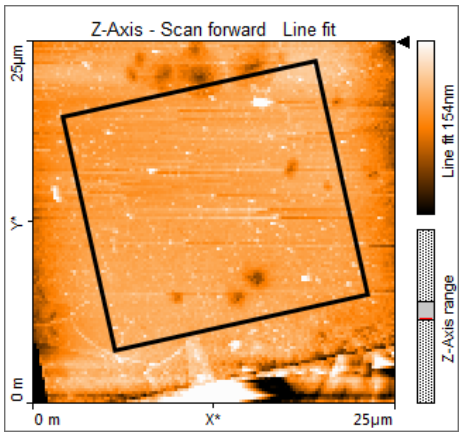

(a) Topographical image of the device E8 (30 μm, 112 kHz). The trench can be seen in the inferior part, showing that the study is made on the mass.

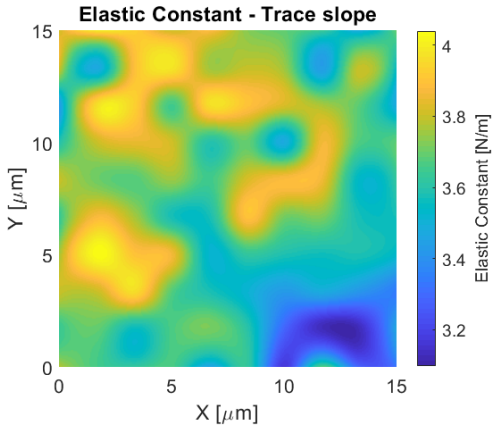

(b) Elastic constant study for the area showed in a), inside the black square. The image is made out of 100 measurements and the elastic constants are more or less homogeneous in that area.

Figure 5.8 – AFM measurements of the Elastic Constant over a square area of 15 μm^2 of the E8 device. The elastic constant shows a homogeneous value around 3.7 N/m.

The same device is also measured with the Digital Holographic Microscope, confirming that the mass has a symmetrical movement while in resonant frequency.

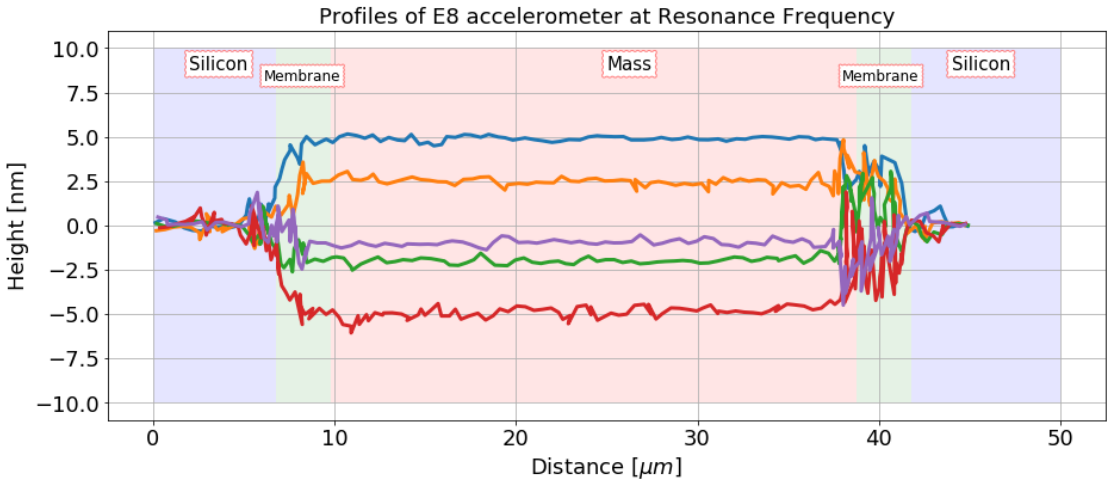

Figure 5.9 – Profiles of the E8 (30 μm, 112 kHz) show the mass oscillates symmetrically for different moments over a period at resonant frequency (112 kHz). Due to the lower amplitude of movement, the measurement is noisier than in the E6 case.

The result from the AFM measurements can be seen in Figure 5.10. There the Elastic Constant (K) extracted is compared with the LDV measurements and the theoretical model.

LDV measurements and Theoretical model					AFM measurements			
Device	Mass	Resonance Frequency	Theoretical Stress	Theoretical Elastic K	AFM (Forward) Elastic K	AFM (Backwards) Elastic K	AFM predicted Resonance	AFM predicted Memb Stress
E6	30 um	50 kHz	115 MPa	3.39	1.18 ± 0.23	1.12 ± 0.27	29 kHz	30 MPa
E8	30 um	113 kHz	588 MPa	17.33	3.65 ± 0.24	4.56 ± 0.29	54 kHz	100 MPa
D8	25 um	177 kHz	1180 MPa	29.5	4.57 ± 0.37	5.94 ± 0.45	74 kHz	160 MPa

Figure 5.10 – Comparison between the AFM measurements and the LDV data and theoretical model. The AFM elastic constants show a lower value than the one expected theoretically. This means that the resonant frequencies of the devices might be located at a lower value and that the ones found are high order harmonics. Unfortunately, no other lower resonances were found in the devices.

5.2.4 Allan Deviation

In Figure 5.4 we performed a frequency sweep for different driving voltages of the Piezo-shaker. To proceed with the study, we need to choose the drive voltage that generates the lowest noise in the device readings. For that goal, we use a powerful tool which is called Allan Deviation. This magnitude is typically used as a metric for the frequency noise of the sensors and was named after Allan et al. [10]. In a general way, it is defined as Equation 5.2.

$$\sigma_y^2(\tau) = \frac{1}{2(N+1)} \sum_{i=1}^{N} (y_{i+1,\tau} - y_{i,\tau})^2 \tag{5.2}$$

Where y_i is the ith measurement of the magnitude y which is taken during an average time τ:

$$y_{i,\tau} = \frac{1}{\tau} \int_{(i-1)\tau}^{i\tau} y(t)\,dt \tag{5.3}$$

The result depends on the integration time τ. In presence of white noise, its value decreases when τ increases. This presents an advantage when compared to the classical variance. Another positive aspect is that the Allan variance converges for most of the commonly encountered kinds of noise.

For the case of resonant-based sensors, y is chosen to be:

$$y(t) = \frac{f(t) - f_{resonance}}{f_{resonance}} \tag{5.4}$$

This is the normalized instantaneous frequency difference to the resonant frequency of the oscillator.

The Allan variance is the best known of the time-domain magnitudes to characterize frequency inaccuracy. From it, we can know the contributions of a different kind of noise: the White Noise (goes like $\tau^{-1/2}$), 1/f noise (goes like τ^0) and the thermal drift (goes like $\tau^{1/2}$).

The White Noise region can be theoretically predicted with the Robbin's formula [11].

$$\sigma_A = \frac{1}{2Q}\frac{N_T}{S}\sqrt{\frac{1}{2\pi\tau}} \tag{5.5}$$

Where Q is the quality factor of the resonator, S is the amplitude of the output signal at the resonance frequency for each drive (in V), N_T is the noise level at the output (seen from the Thermomechanical study) and τ is the integration time.

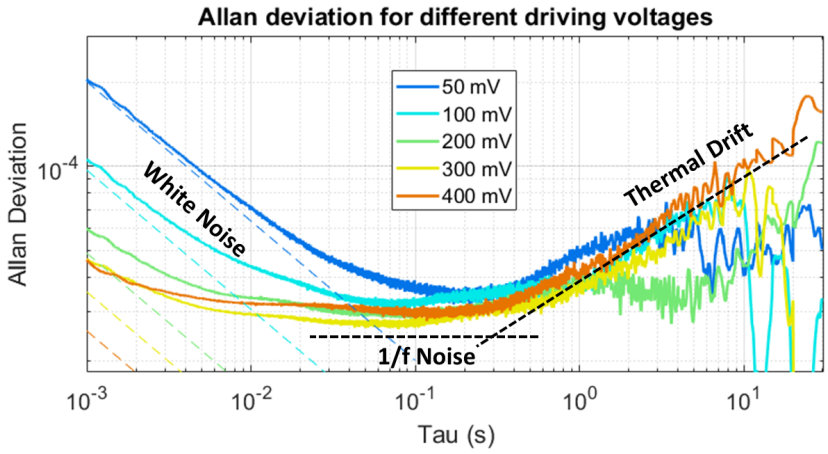

Figure 5.11 – Allan deviation study for the different driving voltages of the piezo-shaker. The different types of noises can be seen and in the White Noise region, the predictions made with Robbin's formula have been plotted in dotted lines. This study helps us to know which driving voltage has the lowest Allan deviation and consequently, the lowest noise. For this specific case (E6 accelerometer, 30 μm and 40 kHz), 300 mV of driving voltage was chosen.

Once the driving voltage for the piezo-shaker is selected, the response of the devices to accelerations can be measured.

5.2.5 Acceleration measurements

As explained previously, to produce an acceleration, a lower frequency signal is inputted into the piezo-shaker, together with the signal that excites the resonant frequency. The acceleration of a signal is the modulus of the second derivative of the sinusoidal wave function. As Equation 5.6 shows, it depends on the signal frequency and its amplitude.

$$Acceleration = (2\pi f_{Accel})^2 \cdot Amplitude \tag{5.6}$$

With the complete explained set-up (Figure 5.2), the variation of the resonant frequency is recorded for 1 minute and the Fourier Transform is performed (see Figure 5.12). Afterwards,

the amplitude of the FFT at the actuation frequency (f_{Accel}) quantifies the effect that the acceleration has on the resonant frequency of the resonator. As the amplitude of the FFT has frequency units, the shift is directly given in Hertz unit.

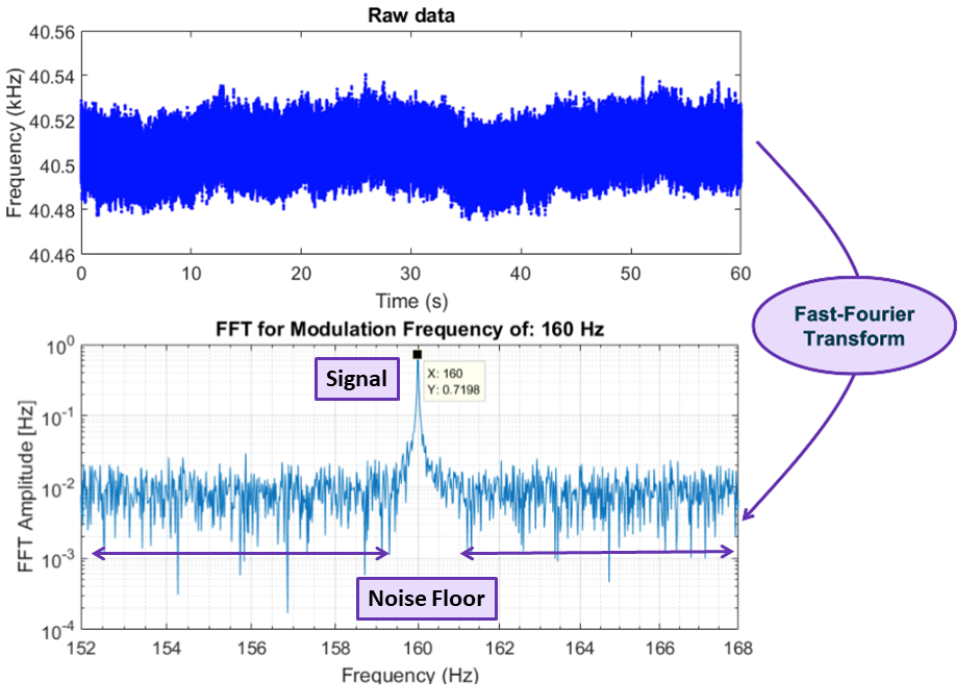

Figure 5.12 – Top: Resonant frequency variation over 1 minute of data acquisition. **Down:** Fast Fourier Transform of the data centered in the acceleration frequency applied in the device. In this example, the resonant frequency shift due to the presence of the external acceleration is seen to be 0.72 Hz.

As seen in Equation 5.6, accelerations can be created by changing the amplitude voltage of the Acceleration signal or by changing the frequency. We do both to see if similar results are obtained.

Accelerations created by changing the signal amplitude

In the experiments of this section, an acceleration frequency of 160 Hz with a 1 g gravitation bias is used. The 160 Hz frequency is commonly used in accelerometer calibrators, as it avoids the 50 Hz noise and in our case is well below the resonant frequencies of our devices.

The responsivity of the devices is shown in [1/a] and in [1/g] units, as normally accelerations

are represented in g units.

$$\mathscr{R}[1/a] = \frac{1}{f_R(g)} \frac{\partial f_R}{\partial a}\Big|_g \qquad \mathscr{R}[1/g] = 9.81 \cdot \mathscr{R}[1/a] \tag{5.7}$$

Acceleration [μg]	ΔF_{res} [Hz]	$\Delta F_{res}/F_{res}$	Responsivity [1/a]	Responsivity [1/g]
320.46	1.2960	$3.20 \cdot 10^{-5}$	0.01017	0.09981
247.60	1.0760	$2.66 \cdot 10^{-5}$	0.01093	0.10725
191.89	0.7937	$1.96 \cdot 10^{-5}$	0.01041	0.10208
136.81	0.5353	$1.32 \cdot 10^{-5}$	0.00984	0.09656
65.92	0.2580	$6.37 \cdot 10^{-6}$	0.00985	0.09658
34.14	0.1380	$3.41 \cdot 10^{-6}$	0.01017	0.09976
16.60	0.0540	$1.33 \cdot 10^{-6}$	0.00818	0.08027

Table 5.1 – Shifts in resonant frequency associated to input accelerations for the device called E6 (F_R = 40 kHz, σ_0 = 75.53 MPa, Mass size = 30 μm x 30 μm x 16.4 μm). The responsivities are calculated as seen in Equation 5.7. We can see that the responsivities are constant for different accelerations and have a value around 0.1 [1/g].

The Figure 5.13 can be obtained by repeating the measurements for many different devices and plotting the resonant frequency shift created by accelerations.

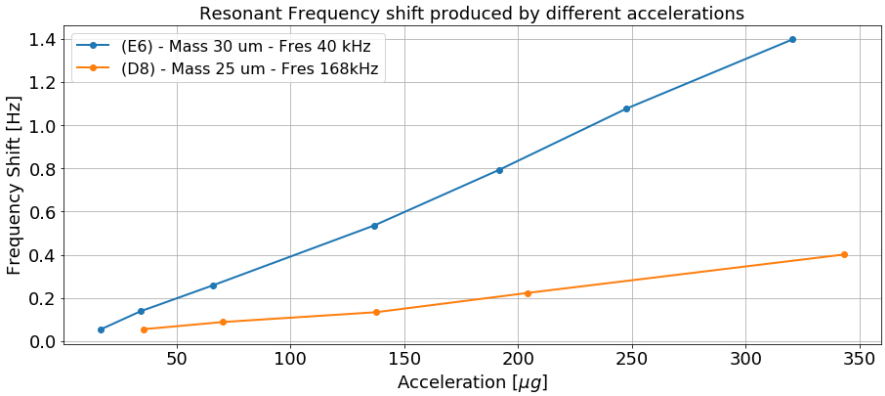

Figure 5.13 – Resonant Frequency shifts produced by accelerations. The study is repeated for different devices. Linearity between acceleration and frequency shifts is observed, which means that the resulting Responsivity calculation is constant for the different input accelerations.

The same study is performed for devices with other characteristics (Figure 5.14). Additionally, the experimental and theoretical responsivities are compared.

Name	Mass	Resonance Frequency [Hz]	Responsivity Average [1/g]	Responsivity std [1/g]	Theoretical Membrane Stress [MPa]	Theoretical Responsivity [1/g]	Ratio Responsivities Experimental/Theory
D6	25um	2.87E+04	2.62E-01	2.80E-02	31.03	1.15E-04	2278
D8	25um	1.68E+05	6.98E-03	1.15E-03	1063.85	2.86E-09	2437236
D2	25um	6.68E+04	1.14E-02	1.26E-03	168.19	7.25E-07	15675
D4	25um	7.47E+04	7.66E-03	1.62E-03	210.32	3.71E-07	20672
E6	30um	4.05E+04	9.75E-02	8.42E-03	75.53	1.19E-05	8164
E8	30um	1.12E+05	2.54E-02	1.44E-03	577.71	2.67E-08	951948
E4	30um	4.69E+04	3.62E-02	5.03E-03	101.29	4.95E-06	7314
F2	40um	3.74E+04	1.65E-02	3.03E-04	87.88	1.41E-05	1171
H8	50um	2.38E+04	1.99E-02	1.51E-03	45.11	1.67E-04	119

Figure 5.14 – Table including the experimental responsivity (Average and Std) and the comparison with the theoretical responsivity. We can see that the experimental responsivity obtained is much larger than the theoretical one. The ratio between responsivities (Experimental and Theoretical) gives large values.

The experimental Responsivity is also compared to the theoretical responsivity obtained with the stresses measured in the AFM. But they are still orders of magnitude lower than the measurements, as seen in Figure 5.15.

			Measured			From Resonant Freq		From AFM
Name	Mass	Resonance Frequency [Hz]	Responsivity Average [1/g]	Responsivity std [1/g]	From theory and Res Fr Membrane Stress [MPa]	Theoretical Responsivity [1/g]	From theory and AFM Membrane Stress [MPa]	Theoretical Responsivity [1/g]
D8	25um	1.68E+05	6.98E-03	1.15E-03	1063.85	2.86E-09	160	8.41E-07
E8	30um	1.12E+05	2.54E-02	1.44E-03	577.71	2.67E-08	100	5.14E-06
E6	30um	4.05E+04	9.75E-02	8.42E-03	75.53	1.19E-05	30	1.90E-04

Figure 5.15 – Comparison of the experimental responsivities with the ones obtained with the AFM study. We can observe that, although they get closer, the difference is still large.

If we consider the experimental results as true acceleration measurements we appear be to able to detect accelerations with high resolution. The studied accelerometers would be far better than the current nonresonant accelerometers (Figure 5.16).

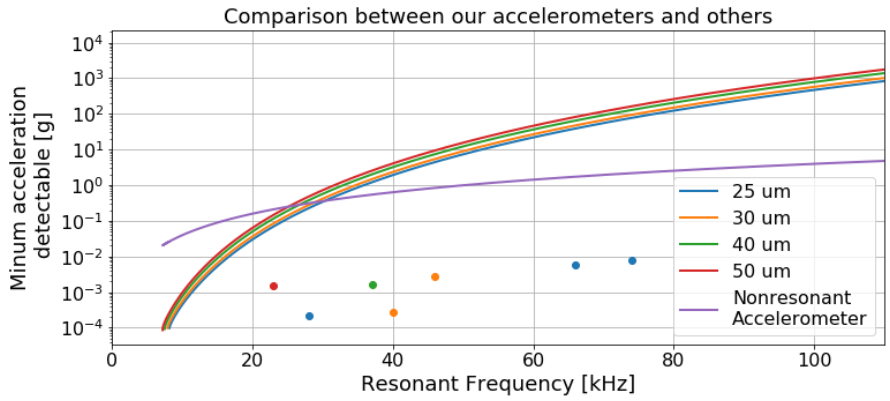

Figure 5.16 – Minimum acceleration detectable with the measured devices (points in the graph). Also plotted, the theoretical model developed and the average nonresonant accelerometer performance. If the accelerometers were truly measuring accelerations, these results would be outstanding.

Different accelerations changing the frequency

We see a linear relation between accelerations and resonant frequency shifts. In this section, accelerations are produced in a different way to see if the results coincide. As seen in Equation 5.6, the acceleration that we input onto the device depends on the amplitude of the signal but also on its frequency (Equation 5.6). For the next measurements, the signal amplitude is fixed and the frequency changes to create different accelerations.

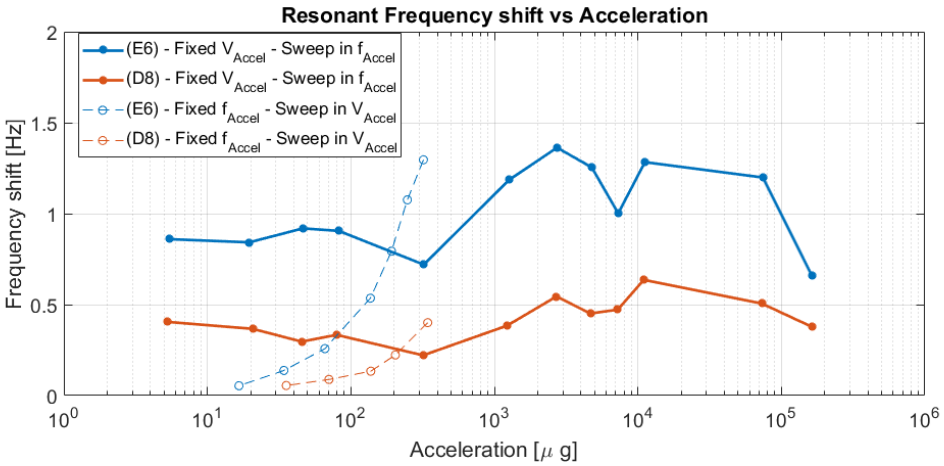

Figure 5.17 – Resonant frequency shifts produced by accelerations created by changing the f_{accel}. For comparing purposes, in dashed lines, the frequency shifts obtained by varying the *Amplitude* of the signal producing accelerations (seen in 5.13). Here we expect a similar behaviour in frequency shift for the two ways of producing accelerations. However, instead of a linear frequency shift, when changing the f_{accel} the frequency shift remains constant. These results demonstrate that the shift of resonant frequency is not due to the accelerations.

In Figure 5.17 we observe that the two ways of producing accelerations do not give the same results. When accelerations are produced varying the *Amplitude* of the signal we observe a linear increase (Figure 5.13). However, when creating accelerations by increasing the f_{accel} we observe a different behaviour: the resonant frequency shifts remain constant. This mismatch indicates that the resonance shifts are not produced by the accelerations.

As a consequence of the different results with the two methods to create accelerations, the responsivity in both cases is also different. Changing the f_{accel} the responsivity is seen to decay with f_{accel}^{-2}, instead of being constant.

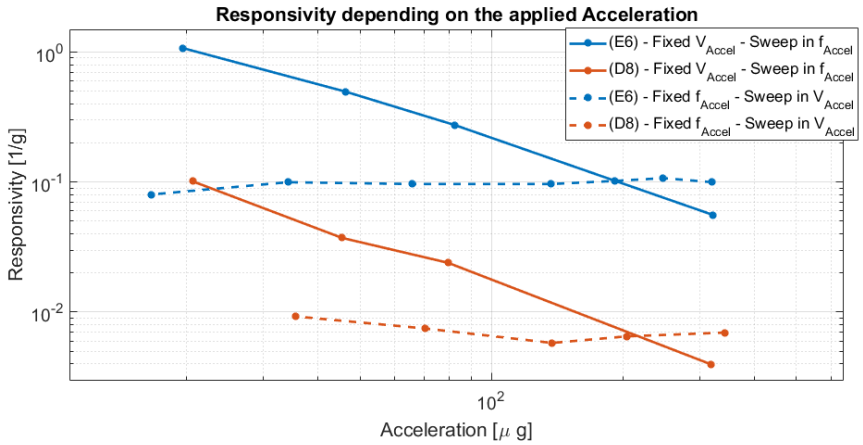

Figure 5.18 – Responsivity for different applied accelerations for devices E6 and D8. Using the two different methods of producing accelerations the results does not match. When creating accelerations by changing the f_{accel}, the resonant frequency shifts were maintained constant and as a consequence, the Responsivity is expected to decrease like f_{accel}^{-2}.

The results shown in 5.17 and 5.18 are really important in this project. From them, we can see that the shifts in resonant frequency are not due to the applied acceleration, but to the applied displacement.

For that purpose, a similar definition than the used responsivity can be created, taking into account the displacement instead of the acceleration.

$$\mathscr{R}_d[1/m] = \frac{1}{f_R(g)} \frac{\partial f_R}{\partial d}\Big|_g \tag{5.8}$$

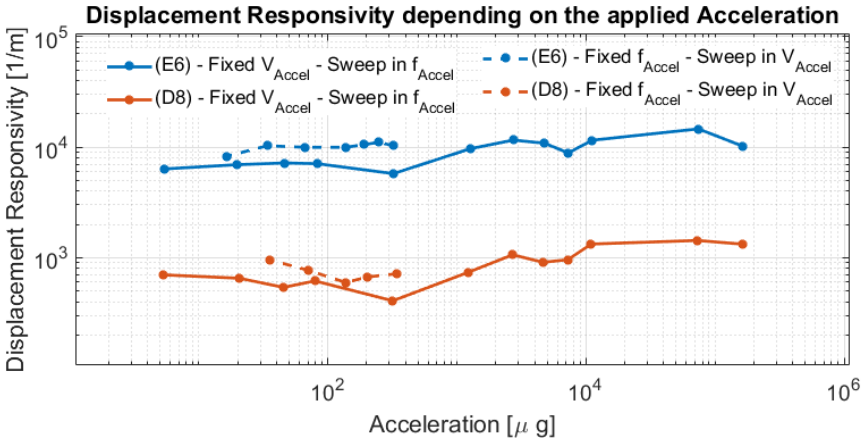

Figure 5.19 – Displacement Responsivity for devices E6 and D8. Using the two different ways of producing accelerations the results match and show a constant behaviour. That means that the effect that changes the resonant frequency is not the acceleration but the displacement.

6 Discussion

6.1 Origin of the resonant frequency shifts

We observe that the resonant frequency shifts seen in the experiments are related to displacements rather than accelerations. In this Discussion, a possible origin for the displacements is debated.

The hypothesis we propose is that the vibrations of the piezo-shaker also create horizontal forces in the silicon surrounding the individual accelerometers. This would then cause variations in the tension of the membranes and therefore affect the resonance frequency. In this situation, the attachment of the chip to the piezo-shaker would have an impact.

To verify the hypothesis, the chip is clamped in numerous different ways on the piezo-shaker. The result that shows the greatest insight is placing the chip in a way that the device under test is hanging, as seen in Figure 6.1. This displays the impact on the membrane stress, which would be caused by horizontal forces in the surrounding silicon.

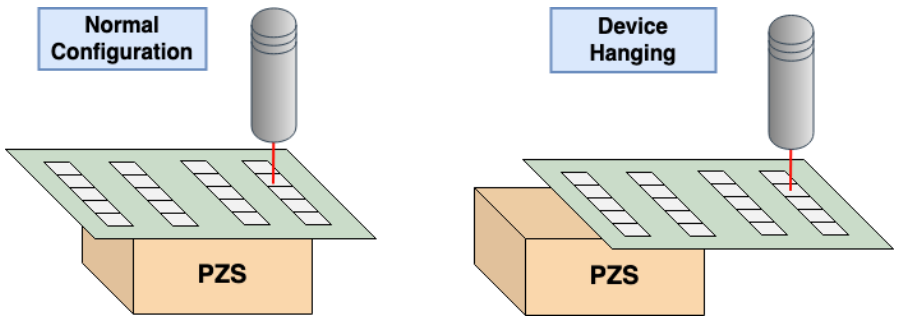

Figure 6.1 – Left: Normal clamped position of the chip to measure the devices. **Right:** Chip clamping to allow the device under test to be hanging. This configuration allows us to see the impact of the horizontal forces on the membrane stress.

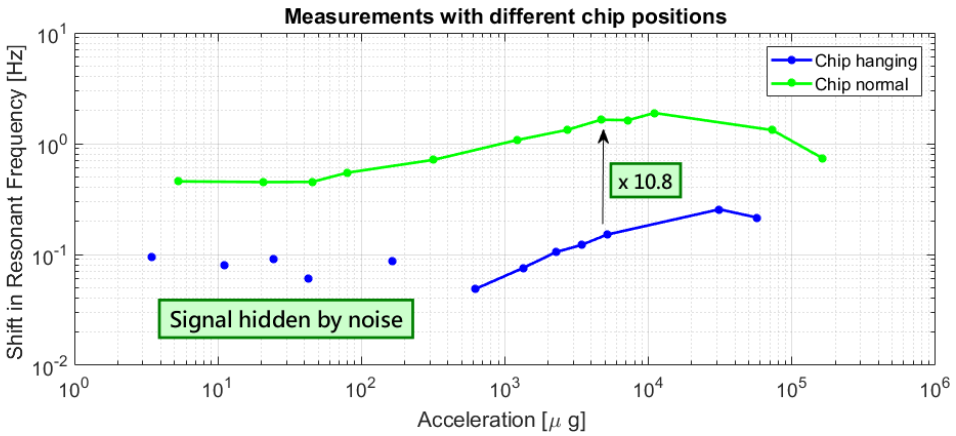

Figure 6.2 – Comparison of the shift in resonant frequency obtained for the different chip positions showed in 6.1. When the device is hanging, the resonant frequency shift observed is reduced by 10 times. The acceleration felt by the device in each position is measured at every moment. The only explanation we can give for the difference is that the detected signal has its origin in the horizontal forces inside the chip.

The chip position on the piezo-shaker affects the measured resonant frequency shifts. The accelerations in each position are calibrated.

The effect of the horizontal forces created by the way the piezo-shaker transmits the vibrations into the chip may be eclipsing the actual effects produced by the acceleration. The response predicted by the theory developed and the simulations performed cannot be experimentally proven.

6.2 New model to describe the displacement effect

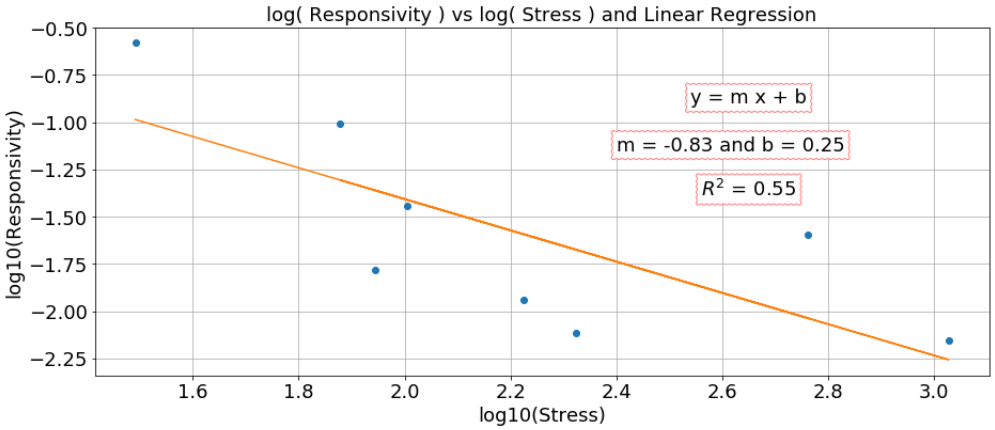

Figure 6.3 – Plot of the Responsivity and the Stress to obtain the relation between the two variables from the experiments. The two variables are related through a power of -0.83. This can be an approximation to the real behaviour that could go with the power of -1.

To model the horizontal forces created in the chip depending on the way the chip is clamped is almost impossible. The only direction we can explore is to plot the experimental data points in a way that we can see the relation of the responsivity with the changes in the membrane built-in stress. As seen in Figure 6.3, the double logarithmic plot shows that the power dependency is close to -1.

$$\frac{\delta f_R}{f_R \cdot \delta z} \propto \frac{1}{\sigma_0} \tag{6.1}$$

More research could be done in that direction. However, this effect is really dependent of the chip position. The authors of this project believe that the way to proceed would be to fabricate new devices where the silicon frame would be more rigid. With this change, the horizontal effects would be minimized.

7 Conclusions

The main objective of this project was to verify the possibility of using the suspended graphene membrane devices as accelerometer resonators. The acceleration would be measured from the resonant frequency shift produced in the device.

The steps followed during the project to approach the objective have been successful and are described as follows.

First, a *theoretical model* was developed (Chapter 3). We extracted the resonant frequency expression for the devices, depending on the membrane parameters and three extra coefficients that take into account the geometry of the whole device. We also introduced the figure that would describe the ability of the sensors to measure accelerations (the Responsivity).

Secondly, using *finite element simulations* (Chapter 4), we evaluated the static displacement of the mass and the resonant frequency of the devices. The study showed the implication of the built-in membrane stress in acceleration detection. The increase of the tension makes it more difficult to detect accelerations, as the device is less perturbed by external forces. The study of the nonlinearities allowed us to determine under which characteristics the devices were working in the linear or nonlinear region. The nonlinear study was crucial for the consequent fitting of the theoretical model to the simulation results. We obtained the geometric constants that completed the theoretical model. Using these new constants we predicted the theoretical responsivity of our devices.

Later, *measurements* were performed into the devices (Chapter 5). The used set-up included a piezo-shaker element located under the accelerometer. Its purpose was to excite the resonant frequency of the device and, at the same time, create a sinusoidal acceleration at low frequency. A Laser Doppler Vibrometer was used to measure the resonant frequency shifts. Other instruments were used to complement the information. For instance, the Atomic Force Microscope and Digital Holographic Microscope. They allowed us to see the movements of the mass and to obtain the membrane elastic constants. The acceleration measurements showed a much larger responsivity when different accelerations were created changing the

signal amplitude. However, when accelerations were produced by changing the modulation frequency, the results showed completely different results. This was proof that the signal that our devices were returning was not proportional to the acceleration but to the displacement.

Finally, in the *discussion* (Chapter 6), a possible hypotheses concerning the origin of the resonant frequency shifts was proposed. This one placed the origin of the signals in the horizontal forces created inside the chip due to the piezo-shaker actuation. Additionally, the first steps into the modelling of these new effect were made by viewing the dependency between Responsivity and Stress.

To conclude, the achievements of this research can be simplified in a list:

- The theoretical model developed matches the behaviour of the finite element simulations. Together, a complete theoretical model was achieved. This allowed us to know the membrane stress and Responsivity of the devices by knowing their resonant frequency.
- We could prove that the signals seen in the experimental measurements were related to the displacement of the piezo-shaker instead of the accelerations produced.
- The principal hypothesis is that the signals observed come from horizontal forces originated in the transmission of the vibrations of the piezo-shaker to the chip. To see only the effect of the acceleration in the measurements, the chip substrate would need to be more rigid.
- The acceleration effects in the resonance frequency were eclipsed by the intra-chip forces. Therefore, the predictions from the theoretical model and the simulations could not be experimentally proven.

Bibliography

[1] X. Fan, F. Forsberg, A. D. Smith, S. Schröder, S. Wagner, M. Östling, M. C. Lemme, and F. Niklaus, "Suspended graphene membranes with attached silicon proof masses as piezoresistive nanoelectromechanical systems accelerometers", *Nano Letters*, vol. 19, 2019. DOI: 10.1021/acs.nanolett.9b01759.

[2] R. Amarasinghe and D. V. D. nad S. Sugiyama, "Nems accelerometers with nanoscale sensing elements", *SENSORS*, vol. 26, pp. 1207–1210, 2010. DOI: 10.1109/ICSENS.2010.5690629.

[3] KTH. (2019). World's smallest accelerometer points to new era in wearables, gaming, [Online]. Available: https://www.kth.se/en/aktuellt/nyheter/world-s-smallest-accelerometer-points-to-new-era-in-wearables-gaming-1.921647 (visited on 08/20/2020).

[4] K. S. Novoselov, A. K. Geim, S. V. Morozov, D. Jiang, Y. Zhang, S. V. Dubonos, I. V. Grigorieva, and A. A. Firsov, "Electric field effect in atomically thin carbon films", *Science*, vol. 306, pp. 666–669, 2004. DOI: 10.1126/science.1102896.

[5] W. M. Zhang, K. M. Hu, Z. K. Peng, and G. Meng, "Tunable micro- and nanomechanical resonators", *Sensors*, vol. 15, pp. 26 478–26 566, 2015. DOI: 10.3390/s151026478.

[6] S. D. Senturia, *Microsystem design*. Massachusetts Institute of Technology: Kluwer Academic Publishers, 2002.

[7] L. G. Villanueva, S. Schmid, and M. L. Roukes, *Fundamentals of Nanomechanical Resonators*. Springer, 2016. DOI: 10.1007/978-3-319-28691-4.

[8] X. Fan, F. Forsberg, A. D. Smith, S. Schröder, S. Wagner, H. Rödjegård, A. C. Fischer, M. Östling, M. C. Lemme, and F. Niklaus, "Graphene ribbons with suspended masses as transducers in ultra-small nanoelectromechanical accelerometers", *Nature Electronics*, vol. 2, pp. 394–404, 2019. DOI: doi.org/10.1038/s41928-019-0287-1.

[9] W. K. Jr. and B. J. McCarraghe, "Modelling and control of interaction forces in nonlinear-stiffness types of contact", *IFAC Proceedings Volumes*, vol. 30, pp. 657–662, 1997. DOI: doi.org/10.1016/S1474-6670(17)44332-1.

[10] D. W. Allan, H. E. Machlan, and J. E. Gray, "National bureau of standards atomic time scales - generation, dissemination, stability, and accuracy", *IEEE Trans. Instrum. Meas*, vol. 21, pp. 388–391, 1972.

[11] M. Sansa, E. Sage, and E. Bullard, "Frequency fluctuations in silicon nanoresonators", *Nature Nanotech*, vol. 11, pp. 552–558, 2016. DOI: doi.org/10.1038/nnano.2016.19.

[12] X. Fan, A. Smith, and F. F. et al., "Manufacture and characterization of graphene membranes with suspended silicon proof masses for mems and nems applications", *Microsyst Nanoeng*, vol. 6, 2020. DOI: doi.org/10.1038/s41378-019-0128-4.

[13] L. Roylance and J. Angell, "A batch-fabricated silicon accelerometer", *IEEE Transactions on Electron Devices*, vol. 26, 1979. DOI: 10.1109/T-ED.1979.19795.